Journal of Sedimentary Research, 2025, v. 95, 133–155
Research Article
DOI: 10.2110/jsr.2024.105

ORIGIN, DISTRIBUTION, AND SIGNIFICANCE OF CEMENTS IN THE MIOCENE VINCHINA FORMATION SANDSTONES, VINCHINA FORELAND BASIN, NORTHWESTERN ARGENTINA

MARIANELA DÍAZ,[1,2] SERGIO A. MARENSSI,[3] AND CARLOS O. LIMARINO[3]
[1]*Universidad Nacional de San Juan, Centro de Investigaciones de la Geósfera y Biósfera, San Juan, Argentina*
[2]*Universidad Nacional de San Juan, Departamento de Geología, Facultad de Ciencias Exactas, Físicas y Naturales, San Juan, Argentina*
[3]*Universidad de Buenos Aires, Instituto de Geociencias Básicas, Aplicadas y Ambientales de Buenos Aires, Argentina*
e-mail: marianelaxy.diaz@gmail.com

ABSTRACT: **The Miocene Vinchina Formation (VFm) is the thickest sedimentary unit of the Vinchina Basin, an Andean broken-foreland basin in northwestern Argentina. Between 16 and 7 Ma, more than 10,000 meters of sediments accumulated in this basin. The sedimentology and compositional characteristics of the unit have been thoroughly studied. However, its diagenetic history is poorly understood. Based on the composition of authigenic minerals and their temporal relationships in seventy-eight sandstone samples, this study presents an interpretation of the diagenesis of the VFm sandstones. Petrographic observations allowed identification of authigenic minerals and their temporal and spatial distribution. X-ray diffraction (XRD) analyses helped differentiate zeolites and clay-mineral species. Using a scanning electron microscope (SEM) with an energy-dispersive spectrometer (EDS) permitted the identification of crystal morphology and the composition of the neoformed phases. Sandstones of the VFm exhibit a diverse arrangement of twelve authigenic minerals, calcite, zeolites, and gypsum being the most prevalent. Their distribution varies geographically throughout the basin due to paleoenvironmental facies distribution, framework clast composition, and diagenetic processes. Carbonate cements dominate the coarser-grained (fluvial) facies in the northern region. In contrast, gypsum is more conspicuous in the finer-grained (lacustrine and playa lake) facies prevalent in the basin's southern sector. Accordingly, clay cements increase from north to south as sediment grain size decreases. The distribution of zeolite cements correlates with the quantity and nature of volcanic clasts. Analcime is abundant in the upper and lower sections and correlates with rhyolitic paleovolcanic clasts. Heulandite and laumontite are frequent in the central and northern areas linked to pulses of andesitic neovolcanic detrital contributions. Finally, deep burial and uplift control the alteration of the neoformed authigenic phases. That is the case of the gypsum to anhydrite, clinoptilolite–heulandite to laumontite, and smectite illitization transformations during the mesogenesis or the formation of secondary porosity during telogenesis. Compositional and textural characteristics of VFm sandstone cements were used to produce a diagenetic model to explain the various pathways, from eogenesis to telogenesis, which occurred in different parts of the basin. Altogether, diagenetic studies suggest that primary composition, depositional-facies distribution, and burial depth were major controlling factors during diagenesis.**

The occurrence of the laumontite–quartz mineral pair in sandstones of the lower part of the VFm suggests that maximum temperatures may have reached a range between 139 and 162 °C. Depending on the sedimentary thickness considered, these values are consistent with either a 13.9 °C/km or a 30 °C/km geothermal gradient.

Thus, establishing a robust depth–time model that considers the effects of progressive unconformities is necessary to determine the basin's paleogeothermal gradient accurately.

INTRODUCTION

Sandstone petrography is a valuable tool for understanding the provenance and tectonic setting in which sediments were formed and deposited (Dickinson 1970; Pettijohn et al. 1972). This is particularly true at convergent plate margins, where foreland basins accumulate large volumes of clastic detritus in a short time (Critelli and Criniti 2021). Foreland basins are tectonically unstable, and continental basin fills tend to be highly heterogeneous. Their foredeeps have high subsidence rates, but sediments have short residence times at depth.

The nature and extent of diagenetic processes depend on several factors, such as primary detrital composition and texture, depositional-facies distribution, geothermal gradient, burial depth, residence time, and fluid chemistry and circulation (Giles 1987; Choquette and Pray 1970; Milliken 1998; McLaughlin et al. 1994; Morad et al. 2000, 2010; Worden and Morad 2000; Worden and Burley 2003; Barbera et al. 2011; Civitelli et al. 2023; Marenssi et al. 2023). For example, early cement precipitation occludes primary porosity and prevents progressive compaction during burial (Marenssi et al. 2023). In addition, the primary detrital composition controls the type of authigenic minerals that develop during diagenesis.

The concept of a diagenetic regime is a broad framework that links diagenetic processes to the evolution of sedimentary basins (Worden and

Published Online: February 2025
Copyright © 2025, SEPM (Society for Sedimentary Geology) 1527-1404/25/095-133

Downloaded from http://pubs.geoscienceworld.org/sepm/jsedres/article-pdf/95/1/133/7113089/10.2110_jsr.2024.105.pdf
by Consejo Nacional de Investigaciones Cientificas y Tecnicas CONICET user

Burley 2003). Three conceptual regimes are commonly recognized, based on a scheme originally developed for limestones by Choquette and Pray (1970): early diagenesis (eogenesis), burial diagenesis (mesogenesis), and uplift diagenesis (telogenesis). Eogenesis refers to all processes occurring in sediments at or near the surface, where environmental factors and clast composition largely control pore-water chemistry. This domain extends to depths of nearly 2 km and temperatures of up to 70 °C (Morad et al. 2000). Paleoclimate significantly influences the detrital composition and near-surface diagenetic environment of continental sandstones (Dutta and Suttner 1986; Suttner and Dutta 1986). Mesogenesis follows eogenesis at deeper burial levels until the onset of initial metamorphic changes (Choquette and Pray 1970). Depending on the residence time of the sediments at depth and the geothermal gradient of the basin, this stage may involve sediments buried several kilometers deep with equivalent temperatures up to 250 °C. Telogenesis is mainly due to the influx of meteoric water during basin inversion and uplift of rocks below the water table (Choquette and Pray 1970).

The Vinchina formation (VFm) is a clastic sequence over 6400 meters thick deposited during the Miocene in the Vinchina broken-foreland basin in northwestern Argentina. Previous studies have assessed the stratigraphic and/or tectonostratigraphic evolution, provenance, geochemistry, and geothermal gradient of the Vinchina Basin and VFm (Ramos 1970; Tripaldi et al. 2001; Collo et al. 2011, 2017; Marenssi et al. 2015; Stevens Goddard and Carrapa 2018; Schencman et al. 2018; Díaz et al. 2019, 2020; Díaz and Marenssi 2020; Wunderlin et al. 2021, 2022). Nevertheless, few focused on the petrographic characteristics of VFm diagenetic history (Díaz 2019; Marenssi et al. 2023).

This research paper presents petrographic information about the main authigenic minerals and their temporal relationships in VFm sandstones. It aims to improve the understanding of the unit's postdepositional history and determine the basin's maximum burial depth and geothermal gradient. This information, in turn, will contribute to a picture of the tectonostratigraphic evolution of the Andean foreland during the shallowing of the Nazca slab beneath the South American Plate. It will also consider the role of external (predepositional) and internal (postdepositional) factors that controlled the development of cements, and establish a diagenetic model for different parts of the basin. The results of this study will provide valuable insights for other foreland basins, many of which are key exploration targets for oil and gas. It aims to enhance understanding of the unit's postdepositional history and ascertain the maximum burial depth, the basin's geothermal gradient, and external factors influencing cement development. The outcomes of this assessment will provide insights applicable to other foreland basins, many of which are prime exploration targets for oil and gas.

GEOLOGICAL SETTING: THE VINCHINA BASIN

The development of the Miocene Vinchina Basin (Fig. 1), situated in northwestern Argentina, was a result of thin- and thick-skinned deformation processes (Beer and Jordan 1989; Jordan et al. 1993; Milana et al. 2003; Japas et al. 2015, 2016) impacting the previously larger Bermejo Basin. Jordan et al. (2001) interpreted this process using the classic foreland-basin model, transitioning from an initial "simple foreland" to a "broken-foreland" phase as deep basement blocks rose through high-angle faults, triggered by the uplift of the Western Sierras Pampeanas, thereby fragmenting the Bermejo Basin into smaller sub-basins, including the Vinchina Basin.

The sedimentary fill of the Vinchina Basin recorded at its southern margin is about 7000 meters thick and comprises various stratigraphic formations. These include the basal, eolian Vallecito Formation (Eocene), signifying the simple foreland stage; the heterolithic Vinchina (Miocene) and Toro Negro (Mio-Pliocene) formations, representing foredeep deposition in the broken-foreland; and the overlying gravelly El Corral Formation (Pleistocene), deposited unconformably in a piggy-back basin (Limarino et al. 2017b). Partial uplift and erosion events occurred at approximately 11 Ma (Marenssi et al. 2000), 7 Ma (Limarino et al. 2010), 4 Ma (Amidon et al. 2016), and $<$ 1.4 Ma (Amidon et al. 2016), forming intraformational unconformities.

Stratigraphy and Sedimentology of the Vinchina Formation

The VFm (Turner 1964) was deposited between roughly 16 and 7 Ma (Ciccioli et al. 2014a; Collo et al. 2017) in a broken-foreland basin amid the Andean orogenesis (Limarino et al. 2001; Ciccioli et al. 2011). Recent advances in dating techniques using U/Pb determinations on volcanic and detrital zircons have refined the understanding of the age of the VFm. Sedimentation ages range between 18 and 7 Ma, reported at various levels in the formation (Ciccioli et al. 2014b; Stevens Goddard and Carrapa 2018; Collo et al. 2017; Amidon et al. 2016).

This formation records sedimentation in alluvial, fluvial, eolian, and lacustrine environments (Ramos 1970; Tripaldi et al. 2001; Limarino et al. 2001; Schencman et al. 2018). Ramos (1970) divided the VFm into lower and upper members based on lithologic features, while Marenssi et al. (2015) further divided it into seven unconformity-bounded units (S1 to S7), representing third-order sequences (Fig. 2). This study utilizes both stratigraphic schemes, with the former providing the broad framework. The latter enables more precise lateral and vertical event correlations.

Ramos (1970) and Schencman et al. (2018) noted significant variations in thickness along the unit's depositional strike. Thickness measurements range from nearly 6500 m in the southern El Yeso section to only 2600 m in the northern Los Pozuelos section. The south and central sections lack an exposed base, while the north section rests unconformably on the Vallecito Formation deposits. Elsewhere an erosional surface separates the VFm from the overlying Toro Negro Formation. Limarino et al. (2010) estimated that this surface eroded up to 1000 m of section at Los Pozuelos (Fig. 2).

Schencman et al. (2018) conducted a thorough paleoenvironmental analysis of the VFm along the Sierra de Los Colorados (La Rioja province), identifying thirteen sedimentary-facies associations representing fluvial, alluvial, lacustrine, and eolian environments. The distribution of these facies allowed them to delineate three sectors in the basin: north, center, and south. Additionally, Schencman (2016) presented paleocurrent measurements indicating variable but mainly southeast-, southwest-, and east-directed paleoflows. However, recent studies by Marenssi et al. (2020) revealed a more complex drainage pattern alternating between stages with axial (north to south) and transverse (west to east) directions.

Schencman et al. (2018) summarized the vertical evolution of paleoenvironments into four distinct stages. Each stage represents a significant shift in environmental conditions and processes. Stage 1 involves the deposition of basal VFm deposits by ephemeral braided fluvial systems, later significantly reworked by the wind under arid conditions with low accommodation space. Stage 2 witnesses a predominance of fluvial transport systems ending in playa lakes, with increased accommodation space under less arid climatic conditions. Stage 3 represents transitioning from braided to meandering river systems and graded to fluvial–eolian interaction environments. Stage 4 is characterized by the development of meandering fluvial systems providing sediment to ephemeral lacustrine systems under variable accommodation space and semiarid climate conditions. This chronological framework is crucial for understanding the paleoenvironmental history of the VFm.

MATERIALS AND METHODS

This study presents the analyses of sandstone samples collected from three sections spanning the depositional dip of the VFm in the Sierra de Los Colorados, located in the La Rioja province of northwestern Argentina (Figs. 1, 2). The study area was divided into three main sectors (north, central, and south) represented by Los Pozuelos, La Troya, and El Yeso sections, where diagenesis assessment is possible due to the extensive

Downloaded from http://pubs.geoscienceworld.org/sepm/jsedres/article-pdf/95/1/133/7113089/10.2110_jsr.2024.105.pdf
by Consejo Nacional de Investigaciones Cientificas y Tecnicas CONICET user

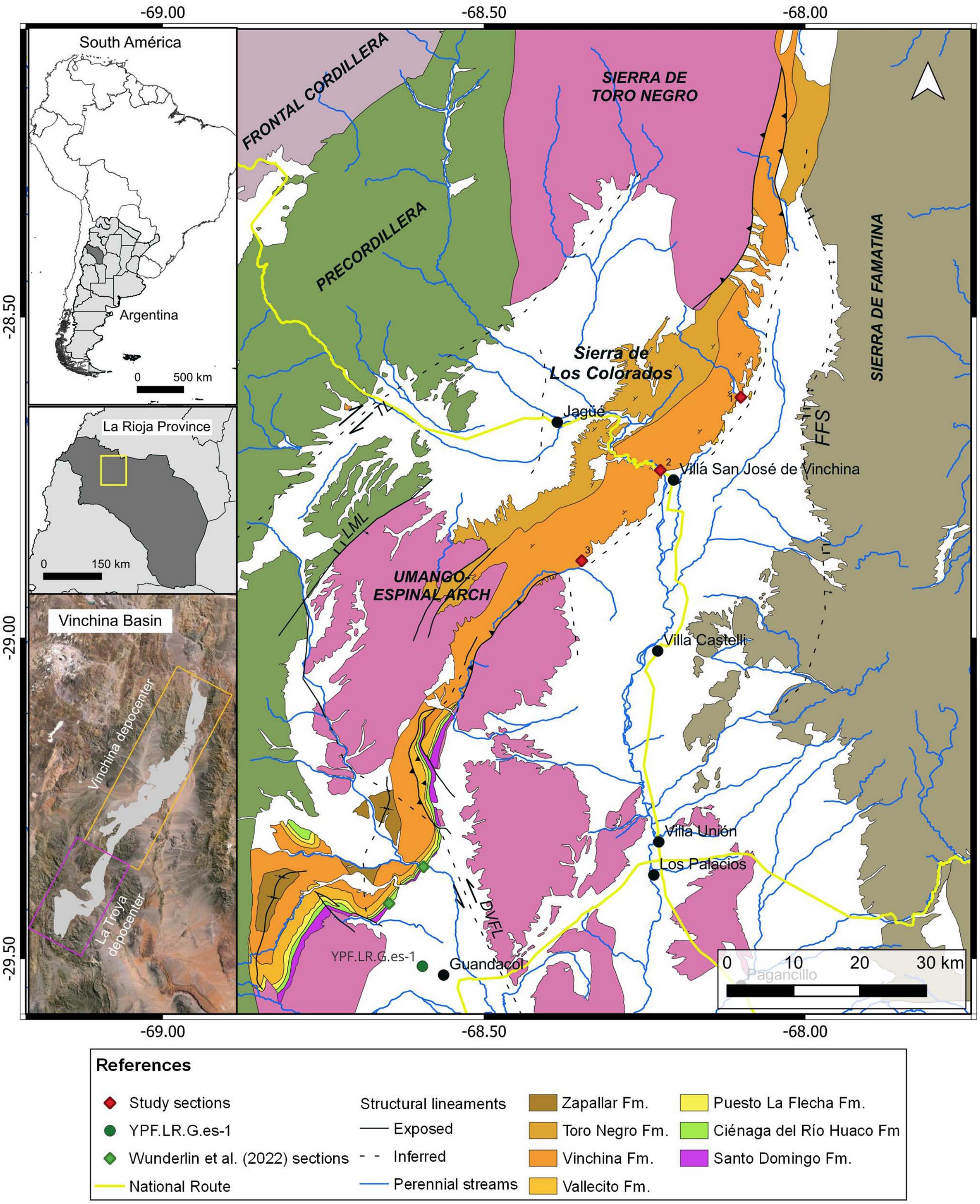

FIG. 1.—Location map showing the main morphotectonic units and structural lineaments. Study sections are indicated by red rhombs: 1, Los Pozuelos (north Sierra de Los Colorados); 2, La Troya (center); 3, El Yeso (south). Wunderlin et al. (2022) study sections are indicated by green rhombs: La Troya (north) and La Flecha (south). YPF well (YPF.LR.G.es-1) indicated by green circle. DVFL, Desaguaero–Valle Fértil lineament; LML, Las Minitas Lineament; TL, Tucumán Lineament.

Downloaded from http://pubs.geoscienceworld.org/sepm/jsedres/article-pdf/95/1/133/7113089/10.2110_jsr.2024.105.pdf
by Consejo Nacional de Investigaciones Cientificas y Tecnicas CONICET user

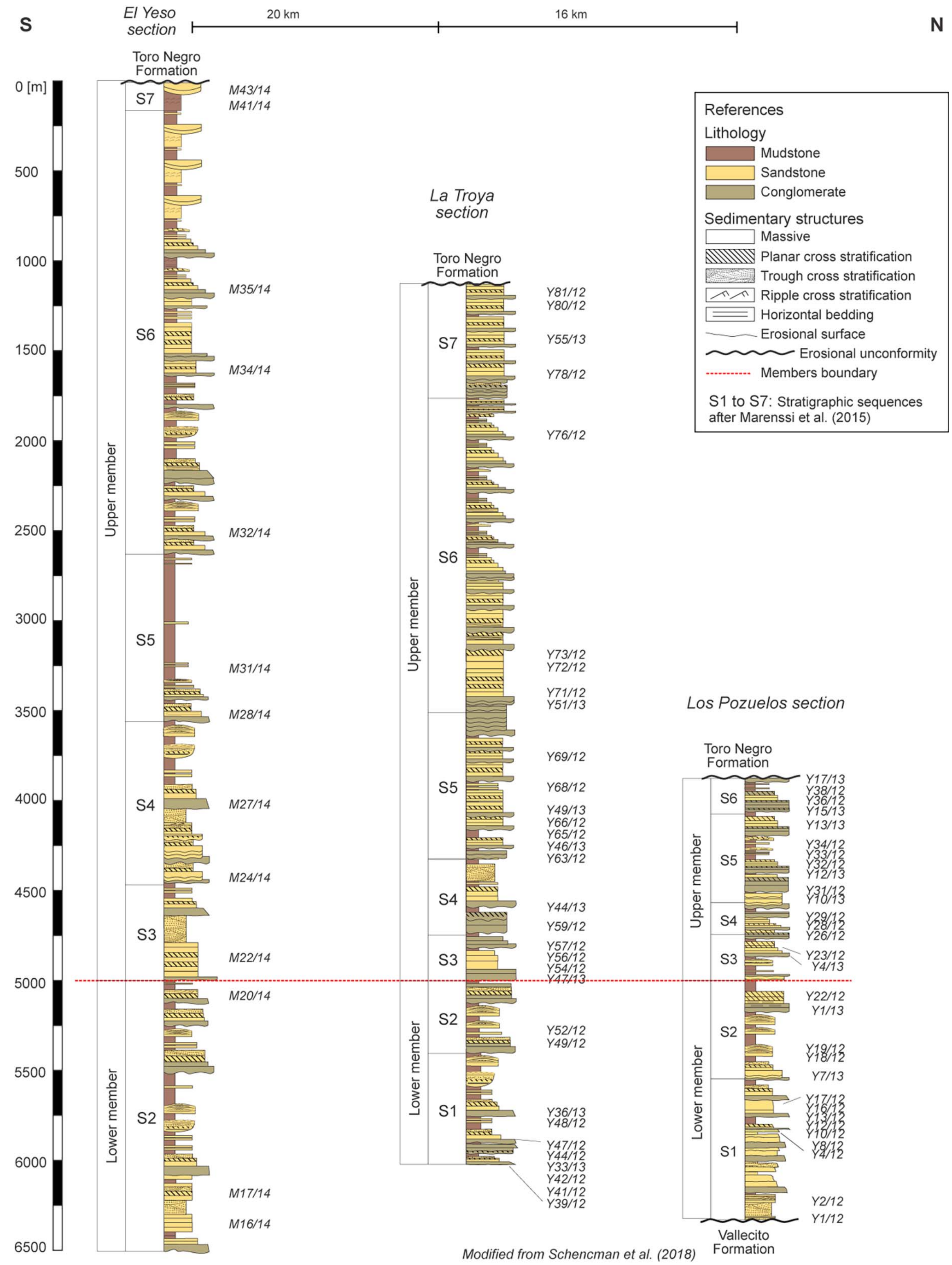

FIG. 2.—Stratigraphic location of the analyzed samples along the three study sections. Sedimentary columns are leveled at the boundary between lower and upper members (red dotted line) of Ramos (1970). S1 to S7 refer to sequences of Marenssi et al. (2015).

Downloaded from http://pubs.geoscienceworld.org/sepm/jsedres/article-pdf/95/1/133/7113089/10.2110_jsr.2024.105.pdf
by Consejo Nacional de Investigaciones Cientificas y Tecnicas CONICET user

exposure of the VFm. Simultaneous sedimentological description and sampling facilitated precise referencing of stratigraphic sample locations in their sedimentological and paleoenvironmental context.

Seventy-eight thin sections of unaltered sandstones were studied under a polarization microscope to determine their detrital modal composition, textural parameters (Table 1), and cement temporal relationships (Table 2). The latter were inferred from spatial associations such as solution vs. precipitation borders, congruent vs. incongruent clast contacts, and cement remnants in poikilitic crystals. Point counting included 300 points per sample, including framework clasts, types of cement, and pores. The framework clast's modal composition was recalculated to 100% of the total framework clasts. Twelve samples (M17/14, M28/14, M35/14, M43/14, Y25/13, Y28/12, Y33/12, Y38/12, Y38/12, Y57/12, Y66/12, Y76/12, and Y81/12) were selected based on their petrographic characteristics. XRD (X-ray diffraction) and SEM-EDS (Scanning electron microscopy–Energy-dispersive spectroscopy) analyses were performed in order to identify authigenic mineral phases and their morphology. XRD analyses were executed at Centro de Investigaciones Geológicas (UNLP-CONICET) with a PANalytical X'Pert PRO diffractometer, using Cu/Ni radiation and generation settings of 40 kV and 40 mA. Bulk-rock on random powders and clay-fraction (< 2 μm) samples were analyzed using the same equipment and parameters. No previous treatment was performed to identify the complete mineralogy of the sample. Clay-fraction assessments included measurements on air-dried, ethylene-glycol solvated, and heated (550 °C during 2 hours) specimens for each sample. The SEM-EDS analyses were performed with an FEI Quanta200 SEM equipped with an EDS detector of the Servicio de Microscopía Electrónica y Microanálisis (SeMFi-LIMF; Facultad de Ingeniería, UNLP, Argentina), at accelerating voltage of 20 kV and a beam current of 1–3 nA. Chemical analyses were carried out with an EDS Detector Apollo 40 and are expressed as oxides percentage.

RESULTS

Sandstone Modal Composition: A Summary

Díaz (2019), Díaz and Marenssi (2020), and Marenssi et al. (2023) assessed the petrographic characteristics of framework clast composition, provenance, and compactional fabrics of VFm. The studied sandstone samples correspond to channel-fill deposits, and are primarily fine- to medium-grained and moderately to poorly sorted, with matrix contents lower than 15% (Díaz 2019). Condensed fabrics were observed which are characterized by the frequent occurrence of long and concave–convex contacts; however, sutured contacts were uncommon, and stylolites were not observed. Floating fabrics and point contacts are related to high cement proportions. The optical porosity, from micropores to macropores, is mostly secondary and produced by the dissolution of framework clasts and cements. It is commonly very low to low (mean 2.3%). However, moderate to very good values were observed in some samples ($> 25\%$; Díaz 2019; Marenssi et al. 2023). Modal composition of samples classifies them as lithic feldsarenites (60.5%), litharenites (22.2%), and feldspathic litharenites (17.3%; Table 1) according to Folk et al. (1970). The distribution of feldsarenites, litharenites, and feldspathic litharenites is similar at the three study sections.

Framework clasts are dominated by quartz, feldspars, and lithic fragments (Fig. 3). Quartz occurs as monocrystalline grains (Fig. 3A), showing flash and undulose extinction. Polycrystalline quartz (Fig. 3B) is very common and, in almost all cases, comprises more than five quartz crystals with evidence of quartz subgrain rotation and grain-boundary migration recrystallization. Feldspars include K-feldspars (KFld), orthoclase and microcline, and plagioclase (Plg). Orthoclase is dominant and appears untwinned or as twinned crystals (Fig. 3C). Microcline is scarce and is recognized by its typical tartan twinning (Fig. 3D). Plagioclase is mainly twinned oligoclase–andesine (Fig. 3E), and less frequently homogeneous andesine. Zoned plagioclases are euhedral to subhedral (Fig. 3F), with low-degree or no alteration. Additionally, they are closely related to the occurrence of andesitic rock fragments.

Lithic fragments include volcanic, plutonic, metamorphic, and sedimentary rocks. Volcanic clasts include rhyolite (VRFa) and less frequently basalt (VRFb). Rhyolite grains exhibit microporphyritic texture, with quartz and K-feldspar phenocrysts (Fig. 3G). Basalt clasts have intersertal texture with abundant twinned plagioclase crystals (Fig. 3H). Unaltered andesite (NVRF) shows microporphyric texture with zoned plagioclase and amphibole as main phenocrysts (Fig. 3I). Plutonic fragments (PRF) correspond to igneous aggregates with granular textures made up of monocrystalline quartz (with both flash and undulose extinction), K-feldspar (orthoclase and sometimes microcline), and muscovite (Fig. 3J). Granitic rocks occur only in coarse to medium sandstones since fine-grained sands rarely preserve complete clasts. Metamorphic grains include both low- and high-grade types. Low-grade (Fig. 3K) are schist, phyllite, and slate. Medium- and high-grade metamorphic rocks (Fig. 3L) correspond to gneiss and migmatite fragments made up of polycrystalline quartz, K-feldspar (commonly orthoclase with minor microcline), and biotite and muscovite. Sedimentary rock fragments are scarce. They include red and green sandstone (Fig. 3M, N) and dark red mudstone (Fig. 3O) clasts. Other components include mica flakes (mostly biotite and lesser muscovite), amphibole (hornblende), pyroxene, zircon, and opaque minerals.

Sandstone Main Types of Cements

The analyzed sandstone samples exhibit cement contents varying from 5 to 30% (average 16%) of total rock volume (Table 2). These include calcite, zeolites (clinoptilolite–heulandite, analcime, and laumontite), chlorite and/or smectite, quartz, iron oxides (hematite), gypsum, kaolinite, and feldspar (albite).

Calcite occurs in two forms. The first one exhibits sparitic texture, forms locally open fabrics, and develops clast displacement by crystal growth (Fig. 4A). Each section contains up to 3% (average 0.6%) of this cement type. Additionally, microesparitic calcite occurs but is restricted to muddy intraclasts (Fig. 4B). The second form of calcite cement comprises large, well-developed crystals, which occasionally form poikilitic textures that envelop small corroded clasts and abnormally open fabrics (Fig. 4C). Additionally, this cement partially or entirely replaced clasts and previous cement (Fig. 4D), sometimes leaving a ghost clast (Fig. 4E). Generally, its contacts with clasts and previous cement (usually rims) are incongruent (segmented rims and corroded clast surfaces), suggesting at least one dissolution period before precipitation. The poikilitic calcite contents vary from 0.1 to 26% (average 5.2%), with the highest participation in the Los Pozuelos and La Troya sections.

Three zeolite mineral species were recognized (clinoptilolite–heulandite, analcime, and laumontite; Figs. 4F, H, 5A, D, 6), constituting pore-filling cement and, less frequently, diagenetic replacement products. Contents of clinoptilolite–heulandite (cli-heu; Fig. 4F) vary from 0 to 16% (average 1.8%) of total rock volume, showing decreasing contents southwards. Cli-heu cement typically fills the intergranular space and occasionally makes up an alteration product of andesitic clast groundmass. This mineral exhibits prismatic or mosaic texture, forming homogeneous aggregates of tiny crystals occluding the pore space and occasionally displacing clast fragments due to crystal growth (Fig. 4G, H). SEM-EDS analyses (Fig. 7A) showed crystal morphology to be hexagonal, flat prisms. Although EDS results indicate that Ca and Mg are the main extraframework cations in the analyzed crystals, it is impossible to differentiate clinoptilolite from heulandite with this information only (Bish and Boak 2001). Thus, this cement will be called clinoptilolite–heulandite throughout the present work. Figure 6A and B depicts XRD diffractograms for sample Y25/13 (Los Pozuelos section). The clinoptilolite–heulandite series was identified in both the bulk-rock and clay fraction analyses by reflections at 8.9–8.98 Å, 5.15 Å, and 4.6–4.68 Å. The

Downloaded from http://pubs.geoscienceworld.org/sepm/jsedres/article-pdf/95/1/133/7113089/10.2110_jsr.2024.105.pdf
by Consejo Nacional de Investigaciones Cientificas y Tecnicas CONICET user

TABLE 1.—*Sandstone composition and textural parameters (modified from Díaz 2019 and Díaz and Marenssi 2020). Qm, monocrystalline quartz; Qp, polycrystalline quartz; KFld, alkali feldspars (including orthoclase and microcline); Plg, total plagioclase (including twinned and zoned plagioclase); VRF, volcanic rock fragments (acidic and basic); NVRF, andesitic neovolcanic rock fragments (Díaz and Marenssi 2020); MRF, metamorphic rock fragments (low-, medium-, and high-grade); PRF, plutonic rock fragments; SRF, sedimentary rock fragments (sandy and muddy clasts); others, includes mica, amphibole, and occasional pyroxene clasts.*

Stratigraphic Location	*Sample*	*Detrital Modes*		*Framework Clast Composition (%)*										Compositional Group (Folk et al. 1970)
		Q:F:L	*Qm:F:Lt*	*Qm*	*Qp*	*KFld*	*Plg*	*VRF*	*NVRF*	*MRF*	*PRF*	*SRF*	*Other*	
Los Pozuelos Section														
Upper member														
S6	Y17/13	*29:14:51*	*25:14:55*	25	4	11	3	26	9	13	2	3	4	Litharenite
	Y38/12	*39:26:32*	*34:26:37*	33	5	14	12	21	1	6	2	2	5	Lithic feldsarenite
	Y36/12	*28:35:33*	*25:35:37*	23	3	22	10	13	1	13	1	2	11	Feldspathic litharenite
	Y15/13	*25:14:59*	*23:14:61*	22	2	9	5	25	7	15	8	5	2	Litharenite
S5	Y13/13	*18:25:50*	*16:25:51*	16	2	8	16	32	11	4	2	4	7	Lithic feldsarenite
	Y34/12	*23:16:54*	*18:16:58*	17	4	6	9	36	4	7	2	1	12	Litharenite
	Y33/12	*36:17:43*	*25:17:55*	22	11	13	2	17	6	12	2	2	14	Lithic feldsarenite
	Y32/12	*27:18:51*	*16:18:63*	14	10	13	4	25	9	4	1	8	11	Lithic feldsarenite
	Y12/13	*30:23:47*	*27:23:50*	25	3	7	15	17	1	11	1	15	6	Lithic feldsarenite
	Y11/13	*35:23:40*	*24:23:51*	24	11	23	0	15	0	15	6	4	2	Lithic feldsarenite
	Y31/12	*34:30:32*	*32:30:34*	32	2	20	10	27	0	4	0	1	5	Lithic feldsarenite
	Y10/13	*46:9:44*	*28:9:62*	27	18	7	2	18	2	17	1	7	2	Litharenite
S4	Y9/13	*38:16:46*	*31:16:53*	31	6	16	0	10	1	19	8	8	2	Lithic feldsarenite
	Y29/12	*18:18:63*	*12:18:68*	11	5	15	1	11	0	39	2	3	13	Litharenite
	Y28/12	*36:9:53*	*29:9:60*	27	7	8	1	16	0	23	8	3	8	Litharenite
	Y26/12	*41:16:42*	*34:16:49*	31	6	13	1	10	0	14	11	3	10	Lithic feldsarenite
Lower member														
S3	Y24/12	*28:20:51*	*24:20:55*	22	4	17	1	10	0	24	6	7	9	Lithic feldsarenite
	Y23/12	*27:31:41*	*19:31:48*	19	7	29	1	3	0	21	14	1	5	Lithic feldsarenite
	Y4/13	*36:24:36*	*31:24:41*	30	5	20	3	12	0	18	3	2	7	Lithic feldsarenite
S2	Y22/12	*37:12:49*	*22:12:64*	21	14	12	0	11	3	19	9	5	8	Litharenite
	Y1/13	*23:35:41*	*20:35:44*	19	3	32	0	0	0	27	7	4	8	Lithic feldsarenite
	Y19/12	*23:36:40*	*17:36:45*	16	5	30	2	4	0	20	6	5	12	Lithic feldsarenite
	Y18/12	*30:41:27*	*28:41:29*	24	2	35	1	3	0	15	4	1	14	Feldspathic litharenite
	Y7/13	*25:27:48*	*16:27:56*	14	7	23	0	5	0	23	4	8	16	Lithic feldsarenite
S1	Y17/12	*37:36:27*	*26:36:37*	25	10	30	4	14	1	6	2	1	7	Feldspathic litharenite
	Y16/12	*28:31:41*	*22:31:46*	22	5	24	6	23	2	10	4	1	3	Lithic feldsarenite
	Y13/12	*13:23:63*	*4:23:73*	4	9	22	0	28	1	24	0	8	4	Lithic feldsarenite
	Y12/12	*23:30:44*	*14:30:53*	13	9	25	4	12	6	16	2	7	5	Lithic feldsarenite
	Y10/12	*28:21:49*	*18:21:58*	18	10	20	1	24	4	2	4	14	3	Lithic feldsarenite
	Y8/12	*37:43:18*	*20:43:34*	20	16	40	2	9	0	8	1	0	5	Feldspathic litharenite
	Y4/12	*33:33:31*	*26:33:38*	26	7	30	2	12	0	10	6	2	5	Feldspathic litharenite
	Y2/12	*45:22:32*	*36:22:41*	36	9	19	2	9	0	15	7	1	2	Lithic feldsarenite
	Y1/12	*33:9:57*	*20:9:70*	19	13	9	0	28	0	18	2	7	4	Litharenite
La Troya Section														
Upper member														
S7	Y81/12	*35:22:42*	*33:22:45*	27	2	17	0	10	1	19	4	1	20	Lithic feldsarenite
	Y80/12	*40:24:35*	*35:24:40*	32	4	20	1	12	1	18	1	0	10	Lithic feldsarenite
	Y55/13	*42:14:43*	*37:14:48*	36	5	13	1	4	0	24	8	7	3	Litharenite
	Y78/12	*45:26:26*	*38:26:32*	33	6	20	2	6	0	11	5	1	16	Feldspathic litharenite
S6	Y76/12	*52:16:29*	*50:16:31*	44	2	13	2	10	0	14	1	1	14	Lithic feldsarenite
	Y74/12	*40:25:35*	*32:25:43*	31	8	21	3	19	1	8	5	1	4	Lithic feldsarenite
	Y73/12	*41:29:28*	*34:29:35*	32	6	26	1	16	2	6	2	1	9	Feldspathic litharenite
	Y72/12	*38:23:37*	*34:23:41*	31	4	20	1	17	1	12	2	2	11	Lithic feldsarenite
	Y71/12	*32:18:50*	*23:18:60*	22	9	16	1	15	2	21	3	9	3	Lithic feldsarenite
	Y5113	*29:20:46*	*23:20:51*	23	5	16	4	26	10	7	2	6	2	Lithic feldsarenite
S5	Y69/12	*29:25:45*	*24:25:50*	23	5	21	2	23	4	9	2	5	7	Lithic feldsarenite
	Y68/12	*27:30:39*	*20:30:46*	18	6	27	0	4	7	10	3	11	13	Lithic feldsarenite
	Y49/13	*18:49:23*	*18:49:23*	16	0	5	38	5	20	1	0	0	15	Feldspathic litharenite
	Y66/12	*30:25:40*	*25:25:44*	23	4	14	9	15	7	8	8	0	12	Lithic feldsarenite
	Y65/12	*10:38:34*	*10:38:34*	9	0	3	31	8	35	1	0	0	13	Feldspathic litharenite
	Y46/13	*41:35:24*	*36:35:30*	34	5	24	9	11	2	7	1	2	5	Feldspathic litharenite
	Y63/12	*51:14:32*	*41:14:43*	40	10	13	1	15	0	13	4	1	5	Lithic feldsarenite
S4	Y44/13	*18:10:72*	*14:10:76*	13	4	8	1	18	2	24	11	11	7	Litharenite
	Y59/12	*35:16:49*	*24:16:60*	24	10	14	1	13	2	21	6	5	3	Litharenite
S3	Y58/12	*28:7:63*	*22:7:69*	22	5	7	0	22	0	25	6	8	5	Litharenite
	Y57/12	*40:19:40*	*28:19:51*	25	10	16	0	21	0	14	1	0	13	Lithic feldsarenite
	Y56/12	*42:23:31*	*26:23:47*	24	16	11	11	10	11	4	1	5	8	Lithic feldsarenite
	Y54/12	*25:13:62*	*13:13:74*	13	12	12	1	21	3	35	0	3	1	Litharenite
	Y47/13	*24:12:63*	*21:12:66*	20	3	11	0	27	3	26	0	6	5	Litharenite

Downloaded from http://pubs.geoscienceworld.org/sepm/jsedres/article-pdf/95/1/133/7113089/10.2110_jsr.2024.105.pdf
by Consejo Nacional de Investigaciones Cientificas y Tecnicas CONICET user

TABLE 1.—*Continued.*

Stratigraphic Location		Sample	Detrital Modes		Framework Clast Composition (%)										Compositional Group (Folk et al. 1970)
			Q:F:L	*Qm:F:Lt*	*Qm*	*Qp*	*KFld*	*Plg*	*VRF*	*NVRF*	*MRF*	*PRF*	*SRF*	*Other*	
Lower member	S2	Y52/12	*54:18:28*	*35:18:47*	33	18	16	1	5	0	20	2	0	7	Lithic feldsarenite
		Y49/12	*40:28:31*	*31:28:40*	29	9	26	1	9	0	17	3	0	5	Lithic feldsarenite
	S1	Y36/13	*46:14:39*	*31:14:54*	31	15	14	0	15	0	19	4	1	2	Lithic feldsarenite
		Y48/12	*47:18:34*	*36:18:45*	31	10	15	0	6	0	21	2	1	13	Lithic feldsarenite
		Y34/13	*34:7:58*	*20:7:72*	20	13	7	0	3	0	45	1	8	3	Litharenite
		Y47/12	*52:21:27*	*38:21:41*	37	14	20	1	19	0	7	2	0	1	Lithic feldsarenite
		Y44/12	*36:24:36*	*27:24:45*	27	9	19	6	17	0	17	2	1	5	Lithic feldsarenite
		Y33/13	*33:13:52*	*27:13:58*	26	6	13	0	19	1	25	6	1	4	Litharenite
		Y42/12	*38:24:35*	*24:24:49*	23	13	13	10	12	3	14	0	6	7	Lithic feldsarenite
		Y41/12	*42:27:30*	*41:27:31*	36	2	23	1	16	2	7	2	0	13	Lithic feldsarenite
		Y39/12	*40:22:37*	*30:22:47*	30	10	14	8	20	0	9	5	3	2	Lithic feldsarenite
El Yeso Section															
Upper member	S7	M43/14	*42:28:29*	*37:28:35*	34	5	24	2	16	0	8	0	2	9	Lithic feldsarenite
		M41/14	*23:26:49*	*15:26:58*	14	8	23	2	15	0	26	4	2	6	Lithic feldsarenite
	S6	M35/14	*45:19:31*	*39:19:37*	36	6	16	2	18	0	10	0	0	11	Lithic feldsarenite
		M34/14	*41:29:28*	*37:29:32*	34	4	22	5	13	0	10	2	0	11	Feldspathic litharenite
		M32/14	*37:39:19*	*34:39:23*	27	3	32	0	7	0	5	1	3	21	Feldspathic litharenite
	S5	M31/14	*28:16:55*	*23:16:61*	22	6	15	0	29	2	14	6	4	3	Litharenite
		M28/14	*30:40:23*	*27:40:26*	22	2	16	16	11	1	5	2	1	23	Feldspathic litharenite
	S4	M27/14	*49:3:49*	*40:3:57*	40	8	3	0	12	0	18	2	16	1	Litharenite
		M24/14	*27:22:49*	*25:22:51*	23	2	21	0	18	0	16	7	4	9	Lithic feldsarenite
Lower member	S3	M22/14	*57:16:22*	*44:16:34*	41	12	13	2	12	0	8	0	0	12	Lithic feldsarenite
	S2	M20/14	*33:21:41*	*25:21:49*	24	8	19	2	29	0	9	2	0	6	Lithic feldsarenite
		M17/14	*49:28:23*	*43:28:28*	40	5	22	4	11	0	8	0	3	9	Feldspathic litharenite
		M16/14	*52:18:25*	*48:18:28*	45	3	17	0	16	0	4	4	0	11	Lithic feldsarenite

second zeolite here recorded is analcime (Anc), which may constitute up to 14.1% (average 2.3%) of total rock volume and is distributed almost equally along the three study sections. This cement presents a macrogranular texture (Fig. 5A, B), comprising large crystals that occasionally form poikilitic textures and open fabrics with congruent clast-cement contacts. SEM studies show a blocky-prismatic crystal morphology (Fig. 7B). XRD analyses (bulk-rock and clay fraction; Fig. 6C, D) of sample M17/14 (El Yeso section) permitted its identification from main diffraction peaks at 5.6 Å, 4.9 Å, 3.43–3.49 Å, and 2.93–2.99 Å. Finally, laumontite (Lmt) occurs in contents that vary from 0 to 21% (average 2.2%), recording its highest values in the La Troya section. Additionally, clast-cement contacts are incongruent in all cases, evidenced by segmented rims and corroded clast surfaces (Fig. 5C, D). SEM studies reveal laumontite's prismatic morphology (Fig. 7C), which is likely associated with the poikillitic texture observed at the polarization-microscope scale. Laumontite displays a "milky" appearance and poorly defined crystal edges occasionally. XRD on bulk-rock and clay fraction of sample Y57/12 (La Troya section) permitted its identification from 9.5–9.52 Å, 6.88 Å, 6.4, 4.24 Å, and 3.63 Å diffraction peaks.

Detrital clay minerals occur as rims on clast surfaces. In all cases, their presence is low, up to 1.0%, increasing southwards. Clay rims are formed by detrital laminae that rest parallel to clast surfaces and are frequently associated with iron oxides (Fig. 5E), and intercalate with syntaxial quartz overgrowths in up to three episodes, filling the pore space in a pulsatory manner (Fig. 5F). This rim is common throughout the sedimentary column and is one of the first minerals of the diagenetic sequence, formed mainly before the precipitation of quartz overgrowths.

At the petrographic-microscope scale, it was not possible to identify the presence of more than one clay-mineral phase. Smectite content was not quantified separately during petrographic observations since it was not differentiated from other clay minerals at the optical-microscope scale. SEM studies showed the occurrence of authigenic, well-developed, highly crenulated, and ragged-edged smectite rims (Fig. 7D) coating grains and filling the pore space. Additionally, highly crenulated smectite exhibits isolated illite threads, evidence for incipient smectite illitization processes (Fig. 7E). Moreover, XRD analyses (Fig. 6) identified the presence of minor contents of probable chlorite (13.13? Å, 7.07–7.15 Å, and 4.6–4.7 Å, the latter probably masked by cli-heu reflection at 4.72 Å). Other clay minerals such as smectite (14.26–14.56 Å at AD, which expands to 15.53–16.83 Å in EG-solvated specimens), I/S (10.54 Å in AD, that expands to 10.75–10.93 Å in EG-solvated), and illite (9.9–9.99 Å and does not expand after ethylene-glycol solvation) are frequent. Thus, it is likely that more than one clay-mineral species makes up the clay rims. Further and more detailed investigations are needed to accurately characterize it.

Quartz cement occurs in three forms: syntaxial overgrowth (0–3%; avg. 0.4%), mega-quartz (0–13%; avg. 0.5%), and micro-quartz (0–0.5%). Syntaxial quartz overgrowth (Fig. 5G) is the most frequent and exhibits variable thickness around monocrystalline and polycrystalline quartz clasts. It is recognized by its optical continuity on quartz grains, both mono- and polycrystalline. Several workers (McBride 1989; Worden and Morad 2000; Emmings et al. 2020) assessed the occurrence of this type of cement, indicating that, in general, quartz overgrowths on polycrystalline quartz clasts are thin, intricate, and hard to follow. Generally, quartz overgrowths on polycrystalline quartz are thinner than those on monocrystalline quartz clasts, since the quartz growth rate decreases with increasing subgrains (Prajapati et al. 2020). Secondary quartz growth projects into the pores; its volumetric significance is moderate and frequently forms thin ridges, which may exceptionally reach 100 μm on monocrystalline quartz clasts. There is usually clay or hematite coating remnants, which allow the identification of the seed quartz clast surfaces. Mega-quartz cement refers to large (20 to 40 μm) well-developed quartz crystal aggregates that fill the pore space (Fig. 5H). Micro-quartz is scarce and is

Downloaded from http://pubs.geoscienceworld.org/sepm/jsedres/article-pdf/95/1/133/7113089/10.2110_jsr.2024.105.pdf
by Consejo Nacional de Investigaciones Cientificas y Tecnicas CONICET user

TABLE 2.—*Sandstone main authigenic minerals and their contents (referenced as % of total rock volume). Clay+Hem rims, indicates undifferentiated clay minerals and hematite coatings; Hem occlusion, pore-filling hematite; Qtz ovgwth, quartz overgrowth; Qtz-mic, microgranular quartz; Qtz-meg, macrogranular quartz–mega-quartz; Fld ovgwth, feldspar overgrowth; Ca (eog), eogenetic calcite (includes macro- and microgranular calcite); Ca mesog, mesogenetic macrogranular calcite; Z-Anc, analcime; Z-Lmt, laumontite; Z-Heu, heulandite; Kaol, kaolinite; Gy, gypsum.*

			Authigenic Minerals (relative to total rock volume)												
Stratigraphic Location	*Sample*	*Total Cements (%)*	*Clay+Hem Rims*	*Hem Occlusion*	*Qtz Ovgwth*	*Qtz-Mic*	*Qtz-Meg*	*Fld Ovgwth*	*Ca (eog)*	*Ca (mesog)*	*Z-An*	*Z-Lmt*	*Z-Heu*	*Kaol*	*Gy*
Los Pozuelos section															
Upper member S6	Y17/13	15.4	0.0	0.5	0.0	0.0	0.0	0.0	0.0	3.0	2.0	0.0	9.0	0.0	0.0
	Y38/12	11.2	0.0	0.5	0.2	0.0	0.0	0.2	1.5	2.5	0.0	0.0	3.5	1.0	0.0
	Y36/12	21.2	0.0	0.2	0.5	0.0	0.0	0.0	3.0	16.0	0.0	0.0	0.0	0.5	0.0
	Y15/13	6.3	0.0	0.0	0.0	0.0	0.1	0.0	2.2	1.0	0.0	0.0	2.5	0.0	0.0
S5	Y13/13	16.9	0.0	0.0	0.0	0.0	0.0	0.0	0.9	2.0	0.0	10.0	3.0	0.0	0.0
	Y34/12	12.9	0.0	0.5	0.5	0.0	0.2	0.2	0.0	3.5	0.0	0.0	5.0	1.5	0.0
	Y33/12	15.8	0.0	0.2	1.0	0.0	0.0	1.0	0.0	0.1	0.0	0.0	11.5	0.0	0.0
	Y32/12	19.7	0.0	2.0	1.0	0.0	0.0	0.5	0.7	9.0	0.0	0.0	5.0	0.0	0.0
	Y12/13	18.8	0.0	0.0	0.0	0.0	0.0	0.0	0.0	1.8	0.0	0.0	16.0	0.0	0.0
	Y31/12	21.4	0.0	3.0	1.5	0.5	0.0	0.2	0.5	13.0	0.3	0.2	0.2	0.0	0.0
	Y10/13	15.4	0.0	0.0	0.0	0.0	0.0	0.0	0.0	12.0	2.4	0.0	0.0	0.0	0.0
S4	Y9/13	26.9	0.0	0.0	0.0	0.0	0.0	0.0	0.0	21.0	4.9	0.0	0.0	0.0	0.0
	Y29/12	25.1	0.0	1.0	0.4	0.0	0.0	0.2	1.0	20.0	0.0	0.0	1.0	0.0	0.0
	Y28/12	9.8	0.0	0.7	0.1	0.1	0.0	0.1	0.3	5.0	1.5	0.5	0.2	0.1	0.0
	Y26/12	6.3	0.0	0.4	0.2	0.0	0.0	0.0	0.3	3.5	0.5	0.5	0.0	0.0	0.0
Lower member S3	Y24/12	27.8	0.5	0.0	0.3	0.0	0.0	0.0	0.0	26.0	0.0	0.0	0.0	0.0	0.0
	Y23/12	19.6	0.0	1.0	0.7	0.0	0.0	0.1	0.4	13.5	1.0	1.0	0.3	0.1	0.0
	Y4/13	7.1	0.0	0.0	0.0	0.0	2.0	0.0	0.5	3.6	0.0	0.0	0.0	0.0	0.0
S2	Y22/12	11.4	0.0	0.3	0.1	0.0	0.0	0.5	0.2	5.0	0.3	3.0	1.0	0.5	0.0
	Y1/13	13.8	0.0	0.0	0.0	0.0	0.0	0.0	2.0	6.0	2.0	3.0	0.0	0.0	0.0
	Y19/12	17.2	0.0	0.5	0.2	0.0	0.0	0.5	0.3	9.0	1.0	2.0	0.2	0.0	2.0
	Y18/12	20.1	0.0	1.5	0.5	0.2	0.0	0.4	0.5	6.0	1.0	4.0	0.5	0.5	3.0
	Y7/13	14.0	0.5	0.0	0.1	0.0	0.0	0.0	3.0	4.9	3.0	2.0	0.0	0.0	0.0
S1	Y17/12	19.5	0.0	1.5	0.2	0.1	0.0	0.5	0.1	4.5	3.5	2.5	1.0	0.1	3.0
	Y16/12	12.1	0.0	0.3	0.2	0.2	0.0	0.4	0.5	4.0	2.5	1.5	1.0	0.0	0.0
	Y13/12	13.8	0.0	0.5	0.3	0.0	0.0	0.0	0.5	7.0	4.5	0.5	0.0	0.0	0.0
	Y12/12	8.6	0.0	0.0	0.2	0.0	0.0	0.0	0.5	3.0	3.5	0.4	0.2	0.0	0.0
	Y10/12	13.0	0.0	0.5	0.0	0.0	0.0	0.0	1.0	4.5	6.0	0.0	0.0	0.0	0.0
	Y8/12	17.6	1.0	1.5	0.5	0.0	0.0	0.0	0.6	3.0	8.0	2.0	0.0	0.0	0.0
	Y4/12	12.5	0.2	1.0	0.3	0.0	0.0	0.0	0.5	2.0	7.0	0.0	0.0	0.0	0.0
	Y2/12	20.3	1.0	1.8	1.0	0.0	0.0	0.0	1.0	5.0	10.0	0.0	0.0	0.0	0.0
	Y1/12	21.2	1.0	1.7	0.5	0.0	0.0	0.0	0.5	8.0	9.0	0.0	0.0	0.0	0.0
La Troya section															
Upper member S7	Y81/12	14.3	0.9	0.0	0.0	0.0	0.0	0.9	0.0	2.0	3.0	4.0	0.0	2.5	0.0
	Y80/12	6.7	0.0	0.0	0.0	0.0	0.2	0.0	0.0	1.5	2.0	2.5	0.0	0.0	0.0
	Y55/13	17.4	0.5	0.5	0.2	0.0	0.0	0.0	0.0	12.8	3.0	0.0	0.0	0.0	0.0
S6	Y76/12	22.8	1.0	1.5	1.0	0.0	0.0	0.0	0.0	7.8	9.0	1.0	0.0	0.0	0.0
	Y74/12	27.0	0.0	0.0	0.1	0.0	0.1	0.0	0.0	23.8	2.0	0.0	0.0	0.0	0.0
	Y73/12	20.4	0.0	0.0	1.0	0.0	0.0	0.0	0.0	7.0	1.0	9.0	0.9	0.0	0.0
	Y72/12	5.8	0.0	0.0	0.3	0.0	0.0	0.0	0.0	1.0	0.0	1.0	2.5	0.0	0.0
	Y71/12	16.0	0.5	0.0	0.2	0.0	0.0	0.0	0.0	10.0	3.0	1.8	0.0	0.0	0.0
	Y51/13	8.6	0.0	0.0	0.0	0.0	0.0	0.1	0.5	2.0	3.0	0.5	1.5	0.0	0.0
S5	Y69/12	18.1	0.5	0.0	1.0	0.0	0.0	0.0	0.0	4.6	0.0	7.0	4.0	0.0	0.0
	Y68/12	18.0	0.5	0.0	0.5	0.0	0.0	0.0	0.0	1.0	0.0	14.0	0.0	0.0	0.0
	Y49/13	15.6	0.0	0.0	0.0	0.0	0.0	0.0	0.0	0.6	0.0	0.0	14.0	0.0	0.0
	Y66/12	8.3	0.5	0.0	0.5	0.0	0.0	0.0	0.0	0.5	0.0	1.0	5.3	0.0	0.0
	Y65/12	18.8	0.0	0.0	0.0	0.0	0.0	0.3	0.0	1.5	0.0	3.0	13.0	0.0	0.0
	Y46/13	15.6	1.0	0.0	0.0	0.0	0.0	0.0	0.0	1.6	2.0	0.0	10.0	0.0	0.0
	Y63/12	14.2	1.0	2.0	0.5	0.0	0.0	0.2	0.0	1.0	0.0	9.0	0.0	0.0	0.0
S4	Y44/13	24.6	0.0	0.0	0.0	0.0	0.0	0.0	0.5	1.0	0.0	21.1	1.0	0.0	0.0
	Y59/12	10.4	0.0	1.0	0.5	0.0	0.0	0.1	0.0	1.0	0.0	7.0	0.0	0.0	0.0
S3	Y57/12	23.6	1.0	1.5	0.6	0.0	0.0	0.0	0.0	3.5	1.0	8.0	7.0	0.0	0.0
	Y56/12	12.5	0.0	1.0	0.1	0.0	0.0	0.0	0.3	0.5	0.0	2.0	7.0	0.0	0.0
	Y54/12	12.4	0.0	0.5	0.4	0.0	0.0	0.0	1.0	2.0	3.0	5.0	0.0	0.0	0.0
	Y47/13	6.1	0.0	0.0	0.1	0.0	0.1	0.0	0.5	1.0	0.0	3.5	0.3	0.0	0.0

Downloaded from http://pubs.geoscienceworld.org/sepm/jsedres/article-pdf/95/1/133/7113089/10.2110_jsr.2024.105.pdf
by Consejo Nacional de Investigaciones Cientificas y Tecnicas CONICET user

TABLE 2.—*Continued.*

				Authigenic Minerals (relative to total rock volume)												
Stratigraphic Location		*Sample*	*Total Cements (%)*	*Clay+Hem Rims*	*Hem Occlusion*	*Qtz Ovgwth*	*Qtz-Mic*	*Qtz-Meg*	*Fld Ovgwth*	*Ca (eog)*	*Ca (mesog)*	*Z-An*	*Z-Lmt*	*Z-Heu*	*Kaol*	*Gy*
Lower member	S2	Y52/12	8.6	0.5	0.5	0.1	0.0	0.5	0.0	0.0	2.0	2.0	3.0	0.0	0.0	0.0
		Y49/12	20.2	1.0	1.0	1.0	0.0	0.0	0.0	0.0	3.2	0.0	14.0	0.0	0.0	0.0
	S1	Y36/13	15.3	0.5	0.3	0.1	0.0	0.0	0.0	3.0	5.0	6.0	0.0	0.0	0.0	0.0
		Y48/12	16.9	1.0	1.0	0.4	0.0	0.0	0.0	1.0	4.0	7.0	2.0	0.0	0.0	0.0
		Y34/13	10.8	0.5	0.0	0.5	0.0	0.0	0.0	1.5	2.0	5.5	0.5	0.0	0.0	0.0
		Y47/12	18.1	1.0	0.0	0.0	0.0	0.0	0.0	0.0	2.0	14.1	0.0	0.0	0.0	1.0
		Y44/12	12.3	1.0	0.5	3.3	0.0	0.0	0.0	0.0	2.5	0.0	4.5	0.0	0.0	0.0
		Y33/13	9.3	1.0	1.5	1.5	0.0	0.0	0.0	0.0	2.5	0.5	1.0	0.0	0.0	1.0
		Y42/12	11.7	0.0	2.0	0.0	0.0	0.0	0.0	3.0	6.0	0.0	0.0	0.0	0.0	0.0
		Y41/12	13.4	0.5	2.0	0.4	0.0	0.0	0.0	3.0	7.0	0.0	0.0	0.0	0.0	0.0
		Y39/12	16.0	1.0	2.0	1.0	0.0	1.5	0.0	0.0	3.5	7.0	0.0	0.0	0.0	0.0
El Yeso section																
Upper member	S7	M43/14	21.4	0.0	0.0	0.4	0.0	13.5	0.0	0.0	2.0	0.0	0.0	0.0	1.5	2.0
		M41/14	22.7	1.0	0.0	0.0	0.0	0.0	0.1	0.0	2.0	0.0	0.0	0.0	0.0	19.0
	S6	M35/14	25.8	1.0	0.0	0.3	0.0	11.0	0.0	0.0	10.0	0.5	0.5	1.5	0.5	0.0
		M34/14	22.4	1.0	0.0	0.5	0.0	2.0	0.0	0.0	13.0	0.4	5.0	0.0	0.0	0.0
		M32/14	18.6	0.5	0.0	0.5	0.0	0.0	0.0	0.0	2.6	0.0	R	1.0	0.0	14.0
	S5	M31/14	11.6	1.0	0.0	0.1	0.0	0.0	0.0	2.5	4.0	0.0	2.0	1.5	0.0	0.0
		M28/14	15.6	1.0	0.5	0.5	0.0	0.0	0.0	0.0	1.6	0.0	2.0	9.0	0.0	0.5
	S4	M27/14	26.7	1.0	2.0	0.0	0.0	0.0	0.0	0.7	1.0	6.0	0.0	0.0	0.0	15.0
		M24/14	14.7	0.5	0.0	0.0	0.0	0.0	0.0	1.5	5.0	3.0	1.7	0.0	0.0	3.0
Lower member	S3	M22/14	24.4	1.0	1.5	0.0	0.0	5.0	0.0	0.0	0.4	1.0	0.5	0.0	0.0	15.0
	S2	M20/14	9.3	1.0	1.5	0.0	0.0	0.0	0.3	0.0	3.0	3.0	1.0	0.0	0.0	0.0
		M17/14	24.6	1.0	1.0	0.6	0.0	5.0	0.0	0.0	3.0	9.0	0.0	0.0	0.0	5.0
		M16/14	30.2	1.0	1.5	0.0	0.0	0.0	0.0	2.0	5.7	10.0	0.0	0.0	0.0	10.0
		Average	**16.3**	**0.4**	**0.6**	**0.4**	**0.0**	**0.5**	**0.1**	**0.6**	**5.2**	**2.3**	**2.2**	**1.8**	**0.1**	**1.2**
		Min.	**5.8**	**0.0**	**0.0**	**0.0**	**0.0**	**0.0**	**0.0**	**0.0**	**0.1**	**0.0**	**0.0**	**0.0**	**0.0**	**0.0**
		Max.	**30.2**	**1.0**	**3.0**	**3.3**	**0.5**	**13.5**	**1.0**	**3.0**	**26.0**	**14.1**	**21.1**	**16.0**	**2.5**	**19.0**

formed by small quartz crystal aggregates, which show a characteristic pin-point extinction.

Iron oxides (hematite and goethite) occur in low contents, up to 3% (average 0.6%) of total rock volume. This mineral has been recognized as grain coatings (Fig. 8A) and pore-filling patches (Fig. 8B). Hematite and goethite coatings are thin, continuous reddish-brown films surrounding framework clast surfaces. Occlusive patchy hematite constitutes dark reddish-brown aggregates that occupy the pore space and exhibit a botryoidal-like texture.

Gypsum cement is present in contents that vary from 0 to 19% (with average of 1.2%). Despite being present in the three study sections, its occurrence is dominant in the southern part of the basin (El Yeso section), as seen in Table 2. Gypsum exhibits coarse granular to poikilitic texture, which may form small concretion-like structures. It occurs in large crystals up to 150 μm long, sometimes preserving grain displacement and deformation of mica laminae due to crystal growth (Fig. 8C). In some cases, giant crystals (up to 250 μm long) surrounding grains form a poikilitic texture, generating a floating fabric. Most contacts between crystals and clasts are congruent, suggesting an early diagenetic origin. However, many incongruent contacts were recorded alongside the poikilitic texture (Fig. 8D), indicating a potential secondary stage of gypsum transformation. Its main diffraction peak showed gypsum at 7.56–7.6 Å (AD and EG-solvated) via XRD analyses (Fig. 6) on sample M17/14 (El Yeso section).

Kaolinite is present in up to 2.5% (avg. 0.1%), being more abundant in the La Troya section. It constitutes pore-filling aggregates of tiny crystals arranged in a mosaic texture (Fig. 8E). Occasionally, it forms partial replacements of feldspars or acidic volcanic rock fragments. The SEM image in Figure 7F depicts well-developed crystalline booklets of probable kaolinite growing from clast surfaces as vermicular stacks. Crystal composition was not determined by EDS analysis, although their morphology is consistent with vermicular kaolinite (Welton 2003).

Syntaxial albite overgrowths occur rarely (0 to 1%; avg. 0.1%) and form thin rim-like growths around alkali-feldspar clasts (Fig. 8F). Clay and hematite remnants on the original seed clast surfaces facilitate their identification.

GEOGRAPHIC DISTRIBUTION OF CEMENTS

The stratigraphic and geographic distribution of the main types of cement are shown in Figures 9 and 10. The volumetrically most abundant cements in the VFm sandstones are carbonate, zeolites, and gypsum (Table 2; Fig. 9). Carbonate and zeolites predominate in the La Troya and Pozuelos sections, whereas gypsum dominates in El Yeso.

Macrogranular calcite is more abundant in Los Pozuelos sandstones, and both its frequency and relative abundance decrease southwards. This distribution is interpreted to be related to the coarse-grained fluvial facies, which are best developed in the proximal (northern) sector of the basin (Schencman et al. 2018). Coarse-grained sediments would have permitted better fluid circulation due to more significant and better-connected pores.

Early eodiagenetic zeolite development seems strongly influenced by the composition of framework clasts. Analcime is present throughout the stratigraphic column (Fig. 9) in the three sections. However, it is more abundant in the lower member and the upper part of the upper member of the formation, where a rhyolite-dominated paleovolcanic petrofacies was identified (Díaz and Marenssi 2020). Clinoptilolite–heulandite is the dominant zeolite in samples from depositional sequence 5 (S5; Marenssi et al. 2015; Fig. 2), overlapping with the neovolcanic petrofacies interpreted from neovolcanic andesitic sandstone framework clasts (Díaz et al. 2019; Díaz and Marenssi 2020). Laumontite geographic distribution is governed

Downloaded from http://pubs.geoscienceworld.org/sepm/jsedres/article-pdf/95/1/133/7113089/10.2110_jsr.2024.105.pdf
by Consejo Nacional de Investigaciones Cientificas y Tecnicas CONICET user

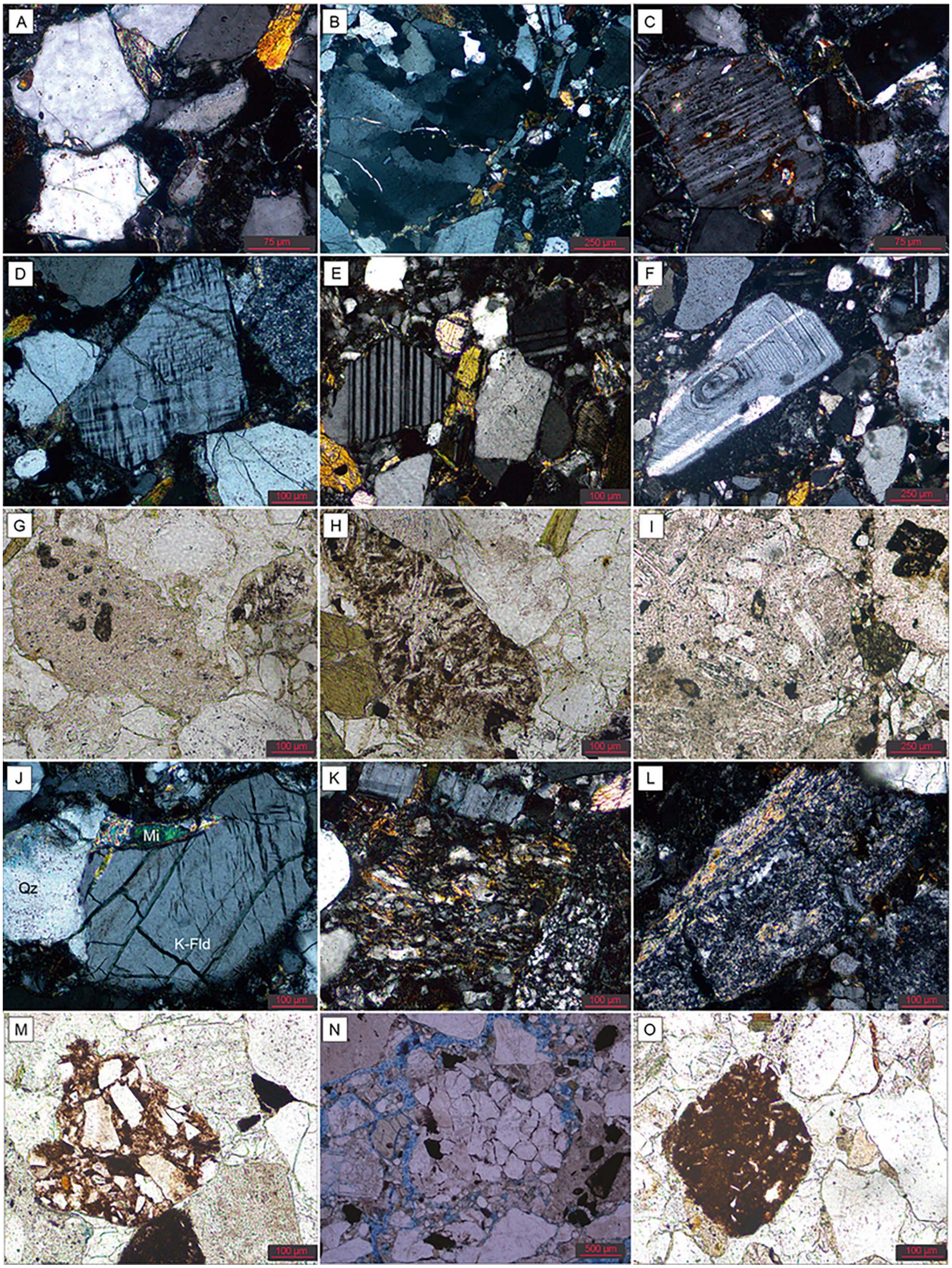

FIG. 3.—Main sandstone framework clasts. **A)** Monocrystalline quartz (Qm), **B)** policrystalline quartz clasts (Qp), **C)** twinned orthoclase, **D)** microcline, **E)** twinned andesine, **F)** subhedral zoned plagioclase, **G)** acidic volcanic rock fragment (rhyolitic), **H)** basic volcanic rock fragment (basalt), **I)** andesitic neovolcanic rock fragment (Díaz and Marenssi 2020), **J)** plutonic rock fragment (granitic; Qz, quartz; K-fld, K-feldspar; Mi, mica), **K)** low-grade metamorphic rock fragment, **L)** high-grade metamorphic rock fragment, **M–O)** sedimentary rock fragments (red sandstone, green sandstone, and mudstone, respectively).

Downloaded from http://pubs.geoscienceworld.org/sepm/jsedres/article-pdf/95/1/133/7113089/10.2110_jsr.2024.105.pdf
by Consejo Nacional de Investigaciones Cientificas y Tecnicas CONICET user

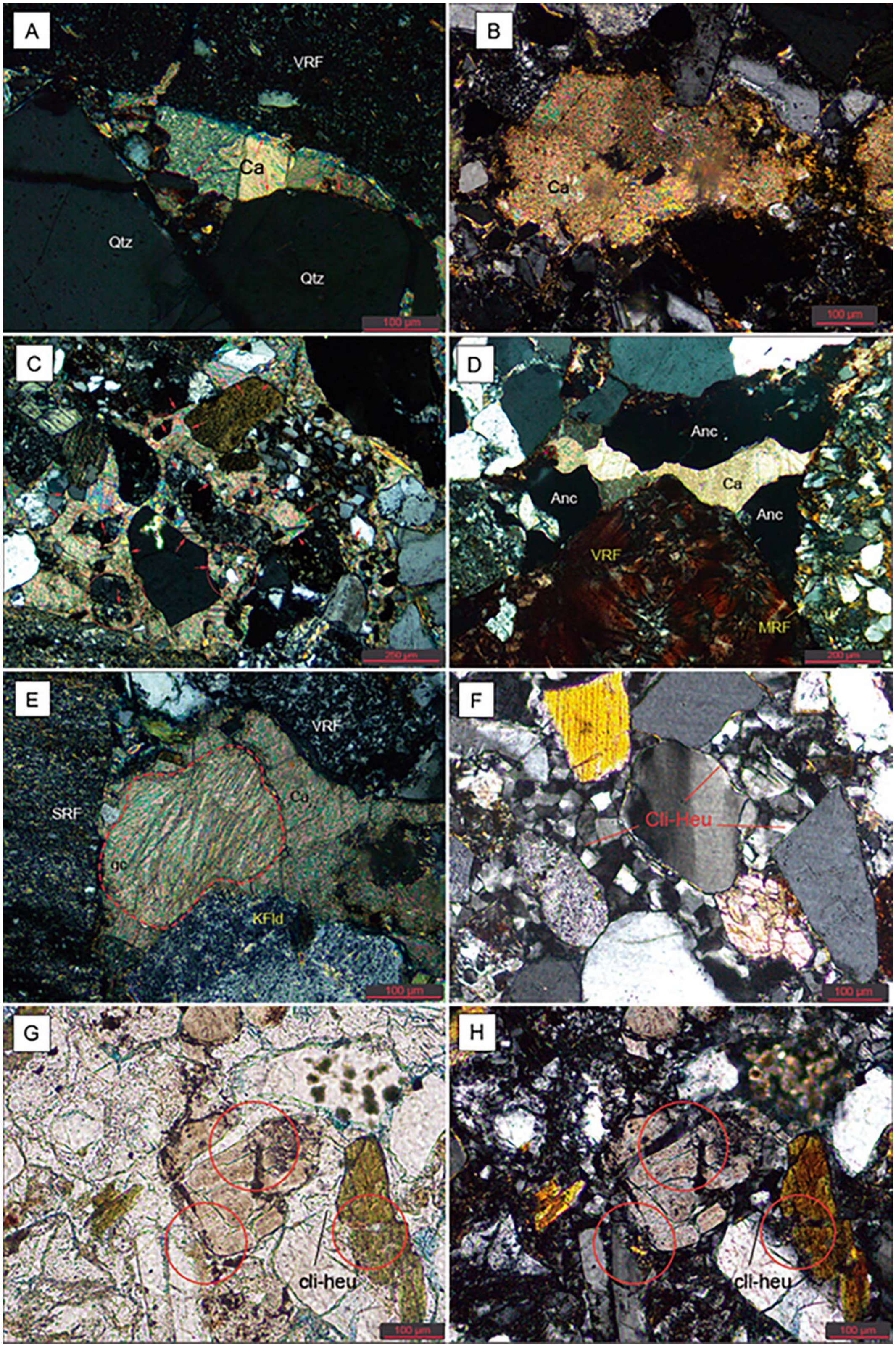

FIG. 4.—Photomicrographs of VFm cements at polarization-microscope scale. **A)** Sparitic calcite (Ca) showing clasts displacement (red arrows) due to crystal growth. **B)** Microgranular or microsparitic calcite affecting muddy intraclasts. **C)** Macrogranular-to-poikilitic calcite involving small corroded clasts (quartz and feldspars; red arrows) forming abnormally open fabrics. **D)** Macrogranular mesogenetic calcite partially replacing previous cement (analcime; Anc). **E)** Macrogranular calcite showing abnormally opened fabric and incongruent clast contacts with rock fragments. In red dotted line, ghost clast (gc) surface remains, highlighted by a difference in calcite textures in and out of the ghost clast limits, suggesting a pseudomorphic replacement. **F)** Clinoptilolite–heulandite (Cli-heu) pore-filling cement with mosaic texture (red lines); notice preservation of clay rims. **G, H)** Clast displacement due to Cli-heu crystal growth, highlighted in red circles. Qtz, quartz; KFld, alkali feldspar; VRF, volcanic rock fragment; SRF, sedimentary rock fragment.

Downloaded from http://pubs.geoscienceworld.org/sepm/jsedres/article-pdf/95/1/133/7113089/10.2110_jsr.2024.105.pdf
by Consejo Nacional de Investigaciones Cientificas y Tecnicas CONICET user

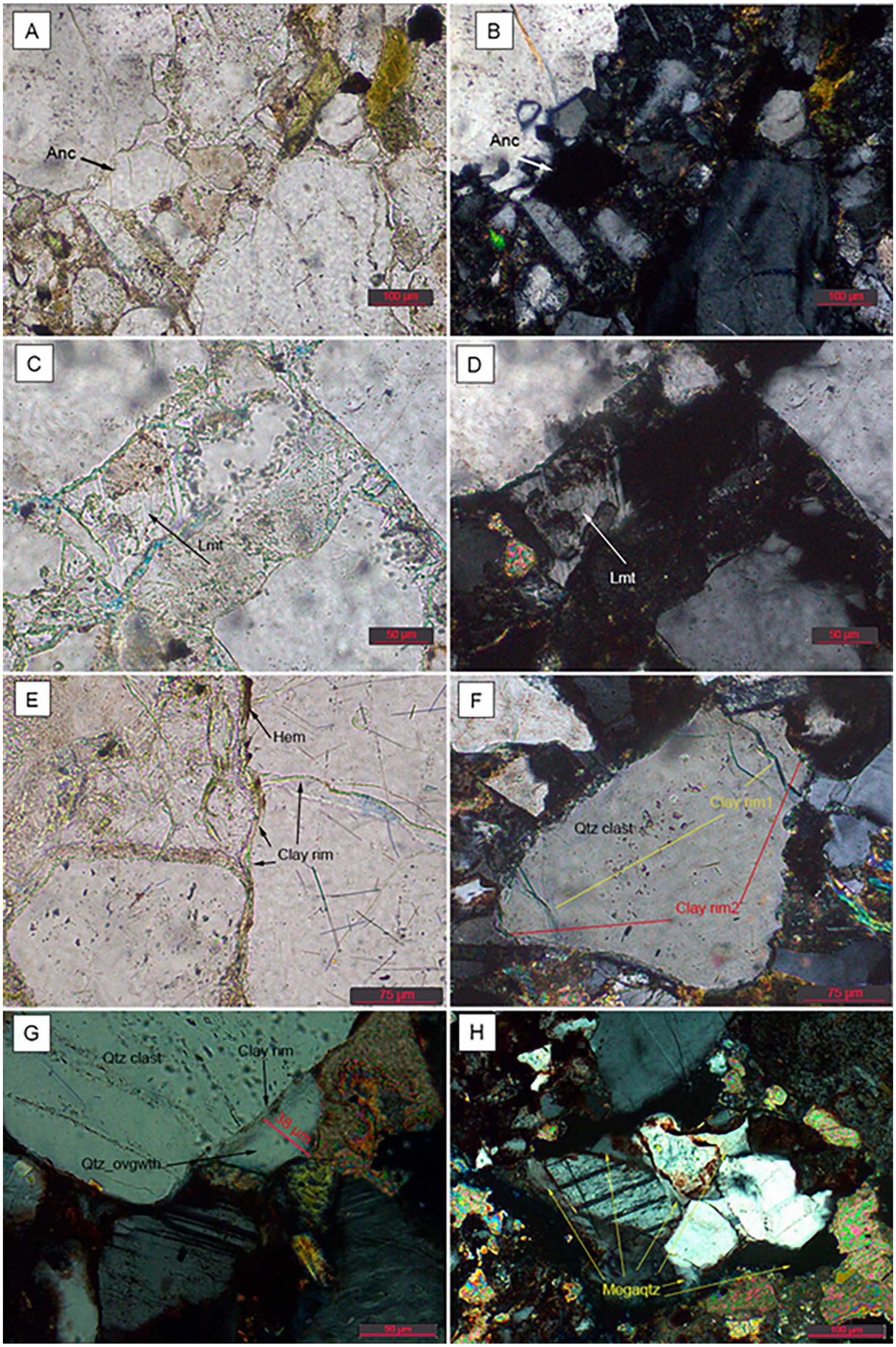

FIG. 5.—Photomicrographs of VFm cements at polarization microscope scale. **A**, **B)** Macrogranular pore-filling analcime (Anc, black/white arrows) forming open fabrics. **C**, **D)** Macrogranular-to-poikilitic laumontite (Lmt, black/white arrows) showing incongruent contacts with corroded crystals of cli-heu. **E)** General view of clay mineral coating quartz framework clasts (black arrows), showing parallel disposition of clay sheets and including Hem, upper photomicrograph arrow. **F)** Alternating clay mineral rims and quartz overgrowths (clay rims 1 and 2), highlighting their sequential layering. **G)** Clear well-developed quartz overgrowth (Qtz_ovgwth; black arrow). The seed clast surface is highlighted by clays+hematite rim. Additionally, macrogranular replacement calcite showing incongruent contacts. **H)** Macrogranular quartz cement (mega-quartz) among quartz and feldspar clasts. Clasts surfaces are highlighted by a residual discontinuous hematite rim.

Downloaded from http://pubs.geoscienceworld.org/sepm/jsedres/article-pdf/95/1/133/7113089/10.2110_jsr.2024.105.pdf
by Consejo Nacional de Investigaciones Cientificas y Tecnicas CONICET user

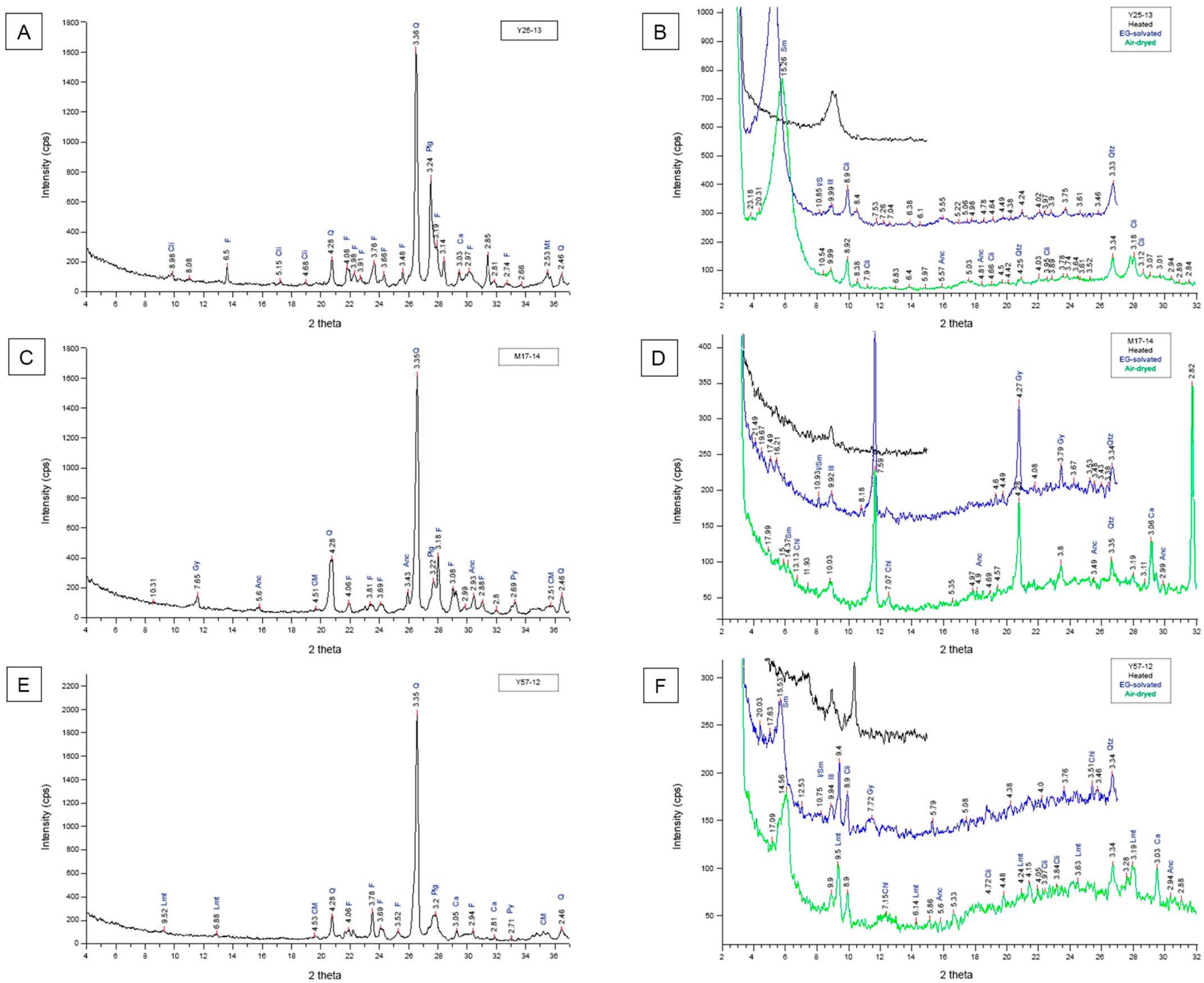

FIG. 6.—XRD graphs on sandstone samples. A, C, E) Bulk-rock. B, D, F) Clay-fraction. Sample Y25/13, **A, B)** Clinoptilolite–heulandite (Cli) is identified by diffraction peaks on d = 8.98 Å, 5.15 Å, and 4.68 Å (bulk-rock) and d = 8.9 Å, 7.9 Å, 4.6 Å, and 3.95 Å (clay fraction). Additionally, illite (Ill), smectite (Sm), interlayered clay-minerals (I/S), and analcime (Anc) were identified in the clay fraction analysis. Sample M17/14, **C, D)** Analcime (Anc) was recognized by its diffraction peaks on d = 5.6 Å, 3.43 Å, and 2.93 Å (bulk-rock) and d = 4.9 Å, 3.49 Å, and 2.99 Å (clay fraction). Gypsum (Gy) is dominant in the clay fraction, and is identified by its main diffraction peaks on d = 7.6 Å, 4.27 Å, and 3.79 Å. Illite, smectite, chlorite, and I/S are also identified. Sample Y57/12, **E, F)** Laumontite is identified by diffraction peaks on d = 9.52 Å and 6.88 Å (bulk-rock) and d = 9.5 Å, 6.14 Å, 4.24 Å, 3.63 Å, and 3.19 Å (clay fraction). Clinoptilolite–heulandite, analcime, illite, smectite, I/S, and chlorite were also recognized. F, alkali feldspar; Q, quartz; Plg, plagioclase; Ca, calcite; Mt, magnetite; CM, clay minerals (undifferentiated); Py, pyrite; Chl, chlorite.

by the previous presence of clinoptilolite–heulandite and its burial (i.e., temperature and pressure) modifications. The authigenic formation of smectite seems to relate to the presence of volcanic-glass alteration, but more studies are needed to better understand its distribution and the composition of its parent material.

Gypsum is dominant in El Yeso section samples (Fig. 9), which generally display a finer grain size than those of the La Troya and Pozuelos sections. According to Schencman et al. (2018), distal fluvial and basinal facies like playa lake, eolian, and distal distributive systems developed in the El Yeso section. The early development of early diagenetic gypsum as the main authigenic phase in this section suggests that it is strongly related to the distal highly evaporitic depositional facies.

The distribution of the main cements of the VFm sandstones suggests that, in addition to burial conditions (pressure, temperature, and fluid migration), other factors controlled authigenic-mineral paragenesis. Considering the paleoenvironmental interpretation of Schencman et al. (2018) and the composition of the sediments (Díaz and Marenssi 2020), we conclude that the main pre-burial controlling factors were:

1. The depositional environment (including climate). It controlled the precipitation of gypsum and iron oxides in the southern (distal) sector during periods of greatest aridity or calcite in the vadose zone associated with proximal to medial fluvial facies.
2. The framework clasts composition. Volcanic clasts provided the parent material for zeolite and smectite. Analcime is associated with paleovolcanic, mostly rhyolitic clasts, while mesosilicic neovolcanic fragments allowed the formation of clinoptilolite–heulandite, which was the precursor for mesogenetic laumontite.

Downloaded from http://pubs.geoscienceworld.org/sepm/jsedres/article-pdf/95/1/133/7113089/10.2110_jsr.2024.105.pdf
by Consejo Nacional de Investigaciones Cientificas y Tecnicas CONICET user

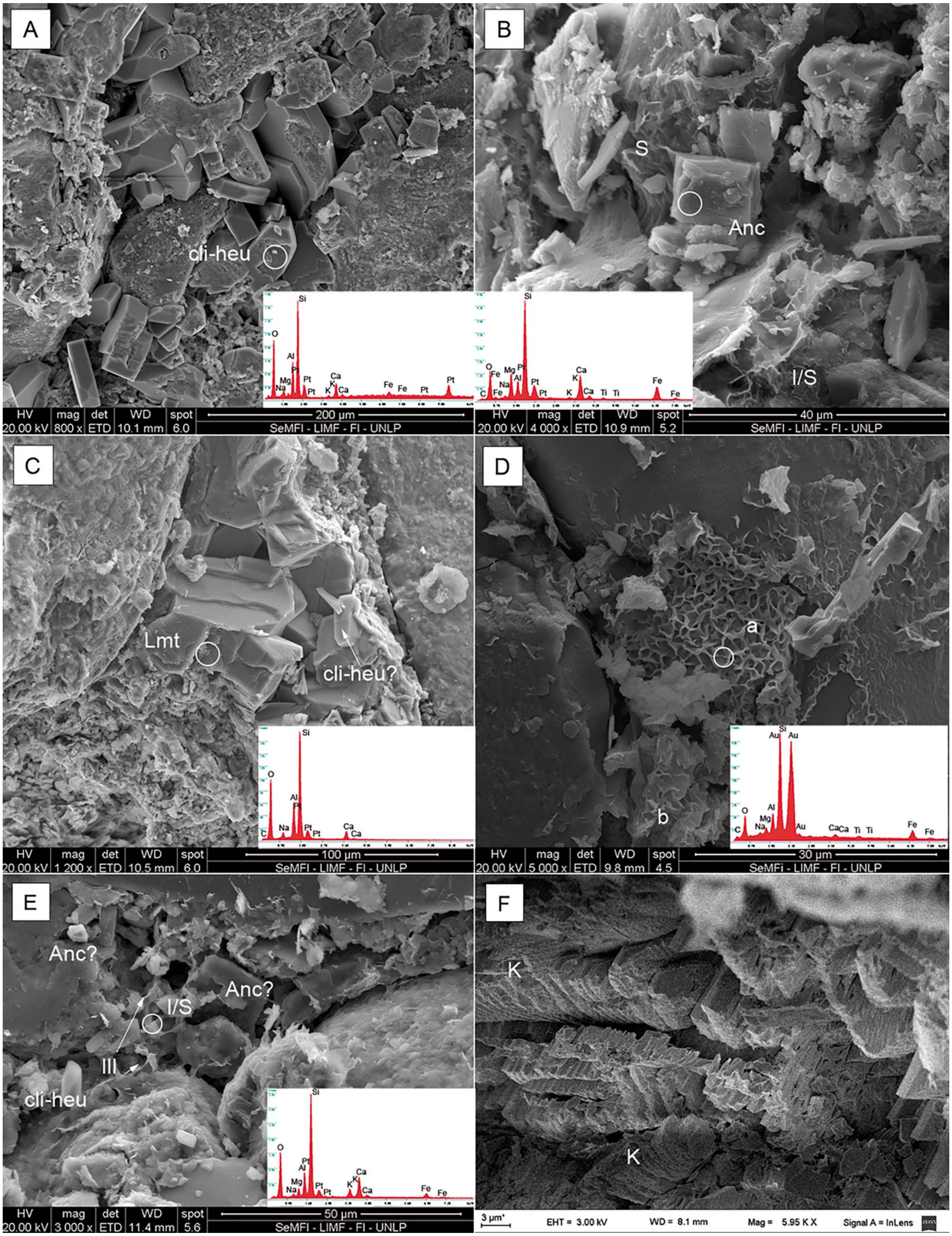

FIG. 7.—**A)** SEM image showing clinoptilolite–heulandite (Cli-Heu) with hexagonal flat prismatic morphology. **B)** Blocky macrogranular analcime (Anc) coexisting with pore-lining authigenic crenulated to ragged-edged smectite (S). **C)** Macrogranular prismatic laumontite (Lmt) with probable cli-heu crystal. **D)** SEM image depicting authigenic smectite is lath-shaped (a), alongside ragged-edged smectite with incipient illite contributes to the formation of illite–smectite (I/S) mixed layers (b). **E)** Illite (Ill) layers on I/S mixed layers coexisting with zeolite (Anc and cli-heu). **F)** Pore-lining vermicular kaolinite (K) showing well-developed booklet morphology.

Downloaded from http://pubs.geoscienceworld.org/sepm/jsedres/article-pdf/95/1/133/7113089/10.2110_jsr.2024.105.pdf
by Consejo Nacional de Investigaciones Cientificas y Tecnicas CONICET user

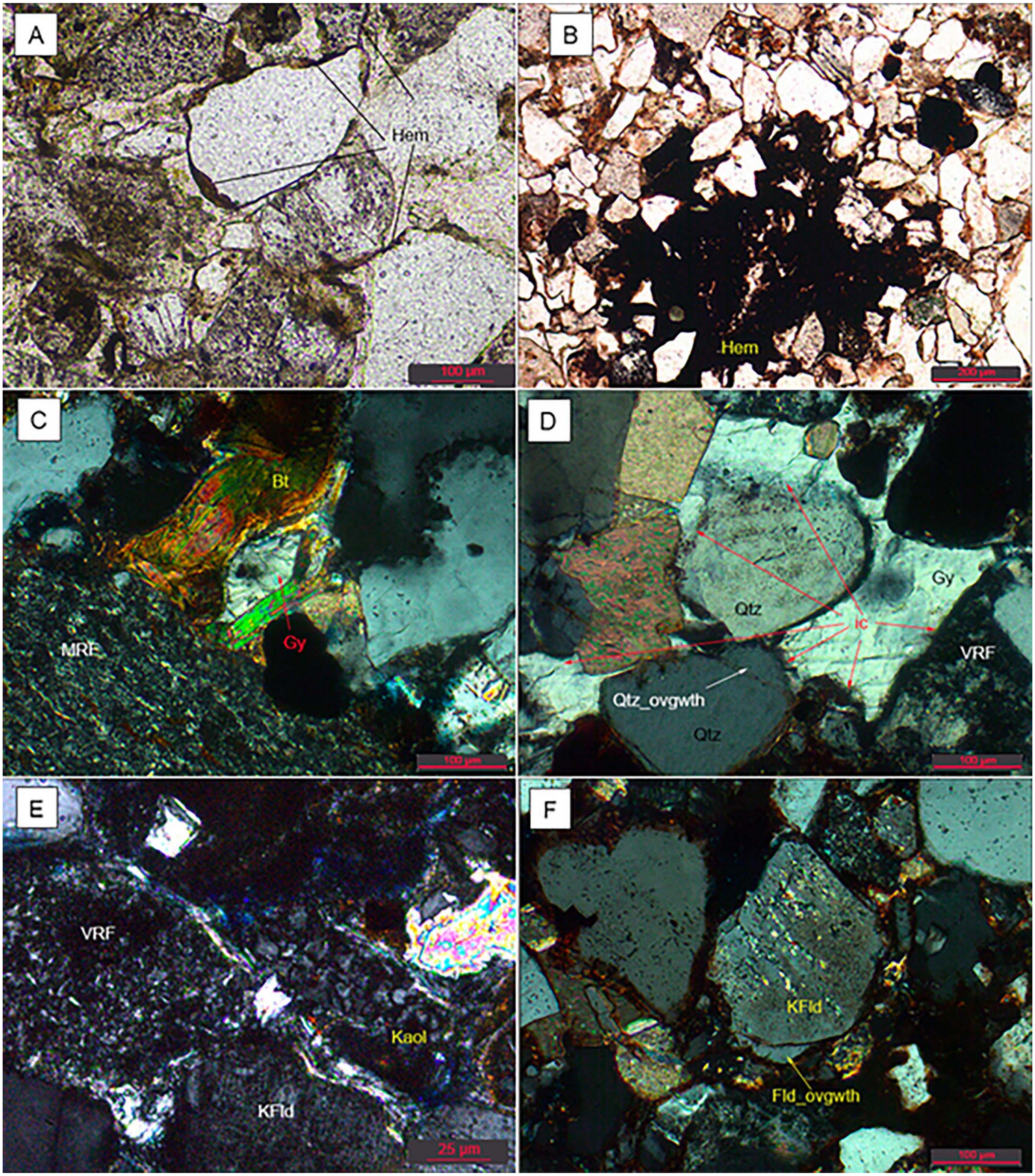

FIG. 8.—Photomicrographs of VFm cements at polarization microscope scale. **A)** Continuous hematite (Hem; black lines) rim on quartz and rock fragments, indicating pre-burial precipitation. **B)** Pore-filling hematite (Hem) forming large patches coexisting with hematite rims. **C)** Eogenetic gypsum (Gy) crystals deforming biotite clast. **D)** Second-generation poikilitic gypsum (Gy) affecting clasts and previous cements. It exhibits incongruent contacts (ic) with quartz clasts, rock fragments, and quartz overgrowths. **E)** Microgranular kaolinite (Kaol) filling up small pore. **F)** Feldspar overgrowth (Fld ovgwth) on a homogeneous K-feldspar clast, with the clast's surface highlighted by a previous hematite rim. Qtz, quartz; Bt, biotite; KFld, alkali feldspar; VRF, volcanic rock fragment; MRF, metamorphic rock fragment.

Downloaded from http://pubs.geoscienceworld.org/sepm/jsedres/article-pdf/95/1/133/7113089/10.2110_jsr.2024.105.pdf
by Consejo Nacional de Investigaciones Cientificas y Tecnicas CONICET user

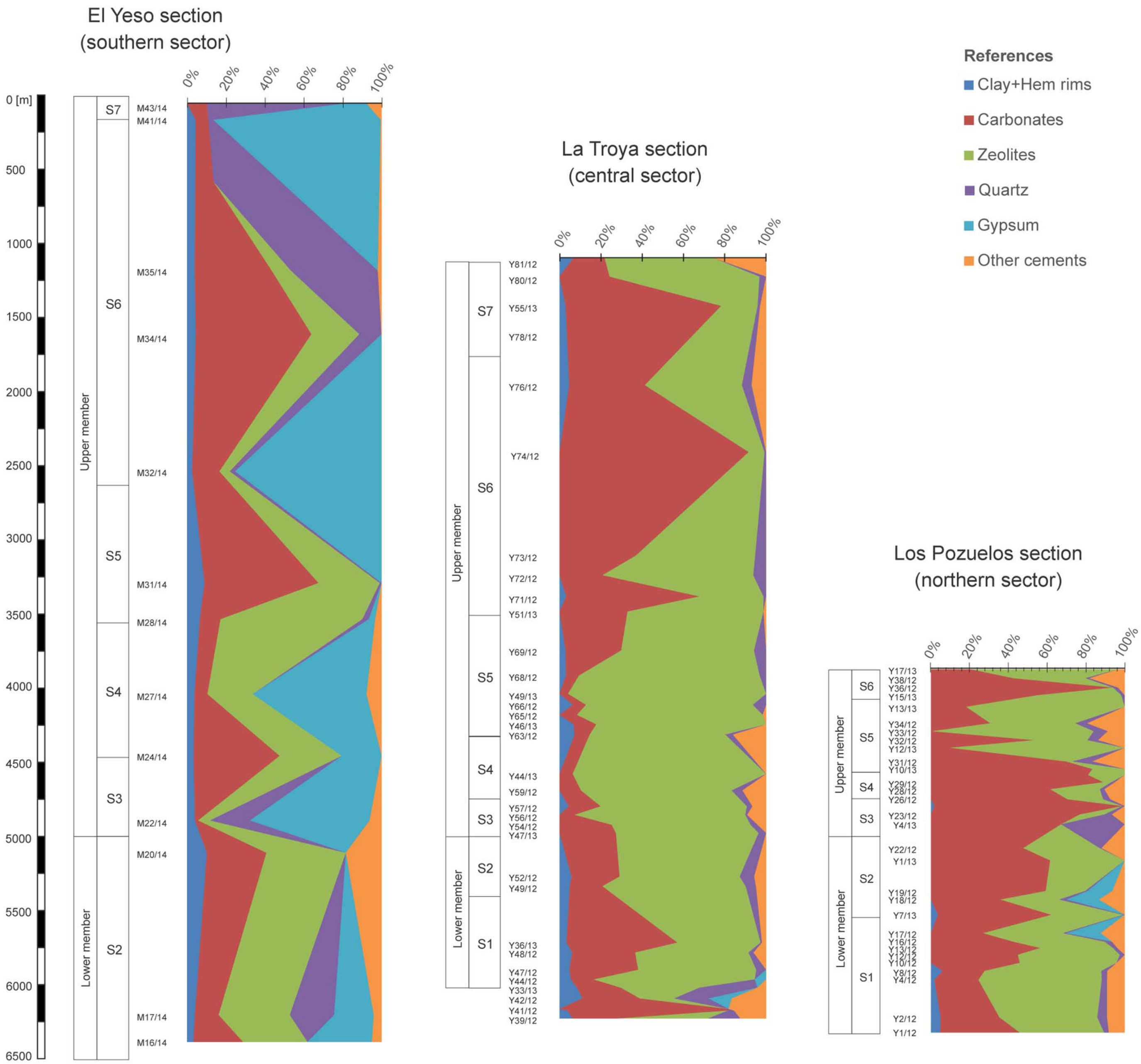

FIG. 9.—100% stacked area chart depicting the stratigraphic distribution of the VFm cements. Gypsum (light blue) development is remarkable in El Yeso section, where it represents up to 80% of the authigenic phases. At La Troya and Los Pozuelos sections, carbonate and zeolite (red and green, respectively) are the dominant authigenic minerals. Although their general content is variable from one section to the other, it increases from the base to the top of VFm. Quartz (purple) and clay+hematite rims (blue) are present in the three sections, although their occurrence increases southwards.

These factors controlled the geographic distribution of cements within the basin. Figure 10 depicts the hypothetical relationships between the most frequent cements and pre-burial conditions for the VFm according to the model proposed by Morad et al. (2000, 2010) and the facies distribution model proposed by Schencman et al. (2018) for the Vinchina basin. The proximal–distal facies distribution controls eodiagenetic processes such as detrital-clay infiltration and calcite precipitation on coarse proximal facies, and coarse granular to poikilitic and concretional gypsum on the fine-grained distal facies. On the other hand, the composition of framework clasts governed the formation of zeolite throughout the basin.

DIAGENETIC PATHWAYS

Based on the previously described cements, we interpret that the VFm sandstones have gone through different diagenetic stages summarized as follows (Fig. 11):

Stage Zero (Pre-Burial Conditions)

This stage is defined as the sediment deposition moment. Petrographic observations indicate that continuous hematite rims would have formed and adhered to the surface of the clasts before burial, probably inherited from the previously formed Permian and Triassic

Downloaded from http://pubs.geoscienceworld.org/sepm/jsedres/article-pdf/95/1/133/7113089/10.2110_jsr.2024.105.pdf
by Consejo Nacional de Investigaciones Cientificas y Tecnicas CONICET user

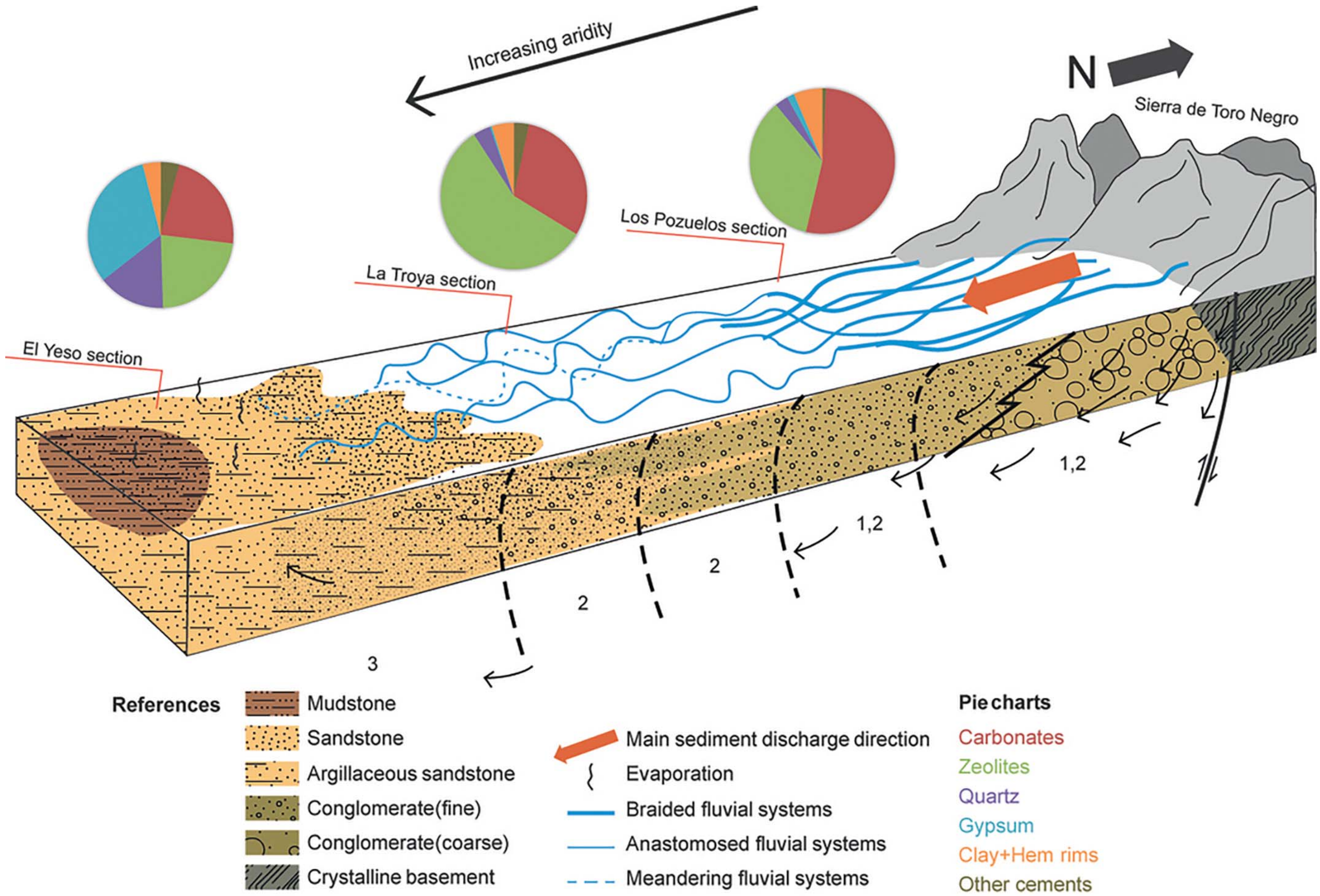

FIG. 10.—Geographic distribution of the main cements along the Vinchina Basin depositional dip (modified from Morad et al. 2000 and Schencman et al. 2018). Orange lines indicate the calculated location of study sections; orange arrow depicts the main sediment dispersal direction, from proximal Sierra de Toro Negro (north) to distal playa lakes (southwards). Pie charts illustrate the average composition of the authigenic phase in each section; carbonate (calcite) and zeolite dominate at Los Pozuelos and La Troya sections, whereas gypsum and quartz do so at El Yeso. Numeric references indicate main diagenetic processes: 1) silicate dissolution, kaolinite formation, and clay infiltration; 2) calcite, quartz, analcime, heulandite, and laumontite precipitation; 3) gypsum precipitation.

red-bed sequences. This stage likely occurred at surface or subsurface temperatures that could have exceeded approximately 20 °C (Valdes et al. 2021), with variations influenced by the latent heat of the vadose zone (Westcot and Wierenga 1974). It is important to notice that this process took place before sediment compaction, as evidenced by petrographic data (continuous hematite coatings).

Stage One (Early Eogenesis)

At this stage, clay and hematite rims would have formed, alternating in a pulsatory manner with quartz syntaxial overgrowth. Kaolinite would have originated from the alteration of detrital K-feldspars and/or volcanic glass, thus sourcing the necessary silica for the previously mentioned quartz rims.

Differences in the dominant pore-filling cements in the southern (situation A) and northern and central sectors (situation B) require a subdivision to better describe the basin's diagenetic history at this stage.

Situation A (Southern Sector).—gypsum precipitation is controlled by pore-water chemistry and sedimentary-environment conditions. Pores were completely occluded by this mineral, preventing the circulation of other fluids. Open fabrics and poikilitic textures indicate that mechanical compaction would have not had a significant effect yet.

Situation B (Central and North Sectors).—Granular calcite occurs, sometimes displacing clasts and separating mica sheets. Crystal growth strength exceeds lithostatic pressure (pre-compaction calcite).

The alteration of the vitreous material in the detrital fraction gives rise to the formation of zeolite, which almost completely blocks the poral space. The formation of analcime or clinoptilolite–heulandite resulted mainly from the Na/Ca ratio in pore fluids. Stage one likely occurred at temperatures ranging from a minimum of 25 °C, as indicated by the presence of kaolinite, quartz overgrowths, eogenetic zeolites, and gypsum, up to a maximum that is defined by the beginning of stage two.

Stage Two (Late Eogenesis)

Previously formed gypsum would have been replaced by anhydrite through a dehydration process (Posnjak 1938; Henderson 1959). This process resulted in formation of secondary porosity (Kasprzyk 1995). Macrocrystalline quartz cement and feldspar syntaxial overgrowths also formed during this stage.

Smectite diagenetic transformation to more ordered types starts during this stage and continues up to the late-mesogenesis stage, at temperatures ranging between 50 and 180 °C (Hower et al. 1976; Hoffman and Hower 1979; Chamley 1994; Pollastro 1993). Consequently, this stage took place between 42 and 50 °C, as indicated by gypsum dehydration and the onset of the smectite illitization processes.

Downloaded from http://pubs.geoscienceworld.org/sepm/jsedres/article-pdf/95/1/133/7113089/10.2110_jsr.2024.105.pdf
by Consejo Nacional de Investigaciones Cientificas y Tecnicas CONICET user

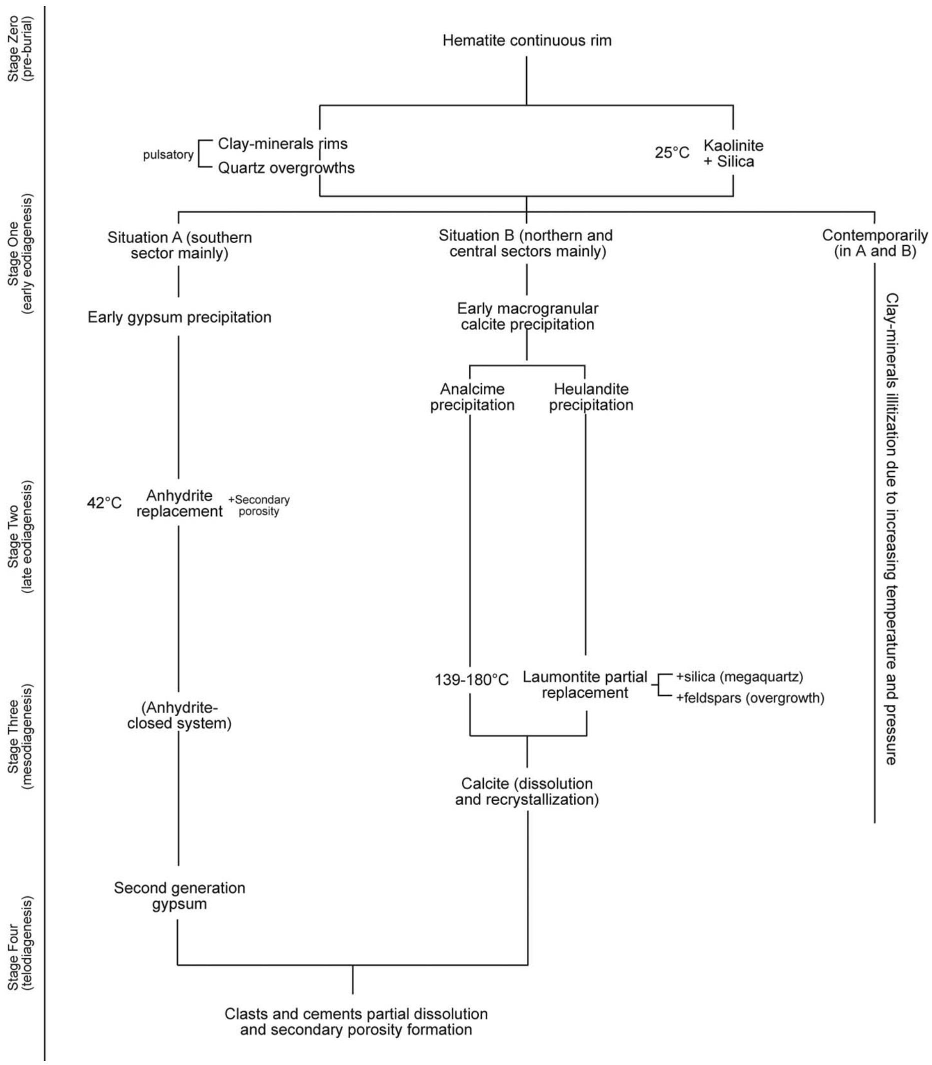

FIG. 11.—Schematic diagenetic-pathways summary. Stage names and temperatures are interpreted based on the authigenic mineral paragenesis and temperature stability intervals.

Stage Three (Mesogenesis)

A dissolution event followed by recrystallization and replacement of the initially formed carbonate with partial to total replacement of previously formed clasts and cements occurred during this stage. Cements formed after this event always show incongruent contacts.

At this stage clinoptilolite–heulandite would transform, at least partially, into laumontite. During this process, Si, Al, Na, and Ca derived from albite dissolution would have been released to solution. The first one would have constituted the necessary material to form mega-quartz cement. The quartz–laumontite paragenesis indicates a temperature range between 139 and 162 °C.

The smectite illitization process continued through this stage, and the transformation of kaolinite into illite by interaction with detrital K-feldspars at 125 °C.

In summary, this stage took place between 125 and 160 °C.

Stage Four (Telogenesis)

During the exhumation of the deposits, the previously formed anhydrite is replaced again by a "second generation" of gypsum, which can be recognized by the presence of incongruous contacts between its crystals and the surrounding clasts. Partial dissolution of cements (such as gypsum, calcite, and chlorite rims) and clasts (phenocrysts of volcanic lithics) results from their interaction with meteoric waters, producing secondary porosity. The temperature at this stage varied as the sedimentary pile was exhumed and the sediments reached meteoric waters.

DISCUSSION

Origin of Cements

Calcium Carbonate (Calcite, Pore-Filling, Occlusion).—Calcite is the most extensive authigenic mineral recorded in the analyzed sandstones. Two main calcite cement types were differentiated based on their diagenetic origin (i.e., eodiagenetic and mesodiagenetic calcite). The eodiagenetic origin of macrogranular and microgranular calcite is evidenced by petrographic characteristics such as clast displacements by crystal growth (macrogranular) and the lithologic restriction to muddy intraclasts of microgranular calcite. This cement may have formed from pore fluids accompanying sedimentation within the vadose zone or water table, where oxic carbonates (Morad 1998) have low Mn and Fe contents and dissolved carbon derives from the decay of plant remains in edaphic horizons and from atmospheric CO_2 (Cerling 1984). A second calcite source, mainly macrogranular calcite, relates to the chemical reactions that result in early quartz overgrowth precipitation (see quartz section below).

Downloaded from http://pubs.geoscienceworld.org/sepm/jsedres/article-pdf/95/1/133/7113089/10.2110_jsr.2024.105.pdf
by Consejo Nacional de Investigaciones Cientificas y Tecnicas CONICET user

Macrogranular mesogenetic calcite combines recrystallization and replacement processes, potentially explaining the floating and ghost textures observed during petrographic examinations (Fig. 4E). Deep micritic or microsparitic cement recrystallization in sandstones can result in poikilotopic calcite (Saigal and Bjørlykke 1987). The replacement of one carbonate cement by another is a typical process during mesogenesis (Boles 1998), possibly explaining the extensive replacement of previously formed cement by late macrogranular calcite.

Zeolite (Clinoptilolite–Heulandite, Analcime, Laumontite, Pore-Filling, Occlusion).—Three authigenic types of zeolite were recognized, making up pore-filling cements. Clinoptilolite–heulandite and analcime likely formed after alteration of volcanic glass during early diagenesis, as evidenced by congruent cement-clast contacts and clast displacement due to crystal growth.

Laumontite formed during a more advanced diagenetic stage (mesogenesis), resulting from the alteration and replacement of heulandite. Numerous studies (Coombs 1954, 1993; Coombs et al. 1959; Ijima and Utada 1966; Boles and Coombs 1975; Cho et al. 1987; Limarino et al. 2017a) have documented the alteration from heulandite to laumontite (microcrystalline quartz, K-feldspar, and albite releasing) through dehydration and cation exchange processes (Coombs 1993). In addition, Coombs (1954) and Cho et al. (1987) reported laumontite and quartz coexistence at temperatures ranging from 139 to 180 °C, whereas Coombs (1993) indicates that this process occurs at depths as great as 9 km.

Hitherto, no unique rule explains the formation of early diagenetic clinoptilolite, heulandite, and analcime by itself. Great efforts were made (Tyrell and Peacock 1926; Coombs 1954, 1993; Coombs et al. 1959; Utada 1965; Ijima and Utada 1966) to comprehend the characteristics governing the different zeolite species formation. The geochemical signal of the parental material and the Si/Al and Na/Ca ratios are the most significant ones. According to our petrographic data, it is probable than analcime formed as an alteration product of rhyolitic to dacitic volcanic glass, whereas clinoptilolite–heulandite did from the alteration of andesitic glass.

Chlorite and/or Smectite (Rims or Coatings).—Chlorite coatings would have formed due to the deposition of chlorite layers parallel to clast surfaces during early diagenesis. Chlorite layers likely formed in response to the alteration of unstable ferromagnesian minerals (Wilson and Stanton 1994), such as olivine, pyroxenes, amphiboles, and biotite. Fe^{2+} and Mg^{2+} cations necessary for chlorite formation may have formed during eogenesis (Boggs 2009). In addition, chlorite may present a detrital origin formed through the physical weathering of metamorphic rocks. According to previous provenance studies on VFm sandstones (Díaz and Marenssi 2020; Díaz et al. 2020), the chlorite source rocks are the Espinal (Turner 1964) and Umango (Arigós 1949) formations, at Sierra de Toro Negro. The contact surface is, in all cases, congruent (i.e., without evidence of dissolution).

The origin of authigenic smectite is related to the alteration of volcanic glass (Chamley 1994; Deconinck and Chamley 1995; McKinley et al. 1999). The VFm sandstone's primary detrital source is volcanic (i.e., rhyolite, basalt, andesite; Díaz and Marenssi 2020; Díaz et al. 2020), all suitable sources of the necessary parental volcanic glass. The observation of pore-filling smectite crystals growing perpendicular to clast surfaces (Fig. 8D) suggests neoformation during eogenesis (Carrigy and Mellon 1964; Galloway 1974; Davies and Ethridge 1975). Authigenic smectite also shows evidence of illitization, such as illite filaments (Fig. 8E). The process of illitization has been studied worldwide (Hower et al. 1976; Hoffman and Hower 1979; Chamley 1989; Pollastro 1993; Moore and Reynolds 1997). It involves the development of a disordered stacking of mixed-layer smectite and illite (I/S) at the time of deposition.

Quartz (Quartz Overgrowths, Coarse- and Fine-Grained Quartz Crystals, Occluding Cement).—Quartz syntaxial overgrowths would have formed early during eogenesis, probably before compaction, and its precipitation had a noticeable effect on porosity. Its early origin is evidenced by its good development, which is several micrometers thick on many occasions. Mesogenetic pore-filling quartz cements have both coarse-grained (mega-quartz) and fine-grained (micro-quartz) texture. The silica required for quartz overgrowth formation may derive from multiple sources, such as alteration of K-feldspars, clays, and lithic clasts, especially those of volcanic origin (Blatt 1979; Boles and Franks 1979; Worden and Morad 2000). Worden and Morad (2000) indicate that silica is a by-product of detrital K-feldspar alteration to kaolinite or illite. Initiation of precipitation of quartz overgrowth has been reported at temperatures as low as 25 °C (Ehrenberg 1990; Walderhaug 1990) and ∼ 40–60 °C (Pagel 1975; Haszeldine et al. 1984; Burley et al. 1989). On the other hand, kaolinite may transform at elevated temperatures (∼ 125 °C; Worden and Morad 2000) to illite releasing quartz by reacting with potassium feldspar clasts. This process constitutes a silica source for quartz cement during mesogenesis. Finally, quartz (+kaolinite and illite) may form during the simultaneous precipitation of carbonate cement such as calcite (Worden and Morad 2000).

Iron oxides (Hematite, Coatings and Pore-Filling).—Hematite rims involve an iron oxide film covering clast surfaces, generally continuous along grain contacts (Fig. 6A, B). This suggests that the patina formed early during eogenesis, before extensive compaction (Limarino et al. 1987). Iron oxides result from the oxidation of Fe^{2+} to Fe^{3+}, which generally derive from the weathering of ferromagnesian minerals such as biotite or amphibole, which are very common in VFm sandstones. Hematite coatings are typical of near-surface diagenesis in continental semiarid fluvial environments with repeated water-table fluctuation (cf. Walker 1967).

Regarding occlusive hematite, it may have formed either by 1) migration of Fe^{2+} during eogenesis and then precipitation as Fe^{3+} (as occurs linked to some coal beds) or 2) total replacement of ferromagnesian minerals where Si and Mg were released to poral fluids. The clast-cement contacts are normally incongruent, suggesting the precipitation of this material after a remobilization event during mesogenesis.

Gypsum (Pore-Filling, Occlusion).—The observation of clast displacement and mica-laminae deformation due to gypsum crystal growth (Fig. 6C) indicates an early diagenetic origin, likely from alkali pore waters in highly evaporitic environments. On the other hand, the recording of incongruent clast-cement contacts (Fig. 6D) suggests that gypsum precipitated after at least one previous dissolution event.

These observations might be explained if Murray's (1964) gypsum diagenetic cycle is considered, which indicates that early gypsum is replaced by anhydrite during burial, followed by anhydrite replacement by gypsum during uplift and erosion of overlying strata. Additionally, laboratory studies carried out by Posnjak (1938) suggest that transformation of gypsum to anhydrite can occur at temperatures as low as 42 °C in distilled water, with decreasing temperatures as water salinity increases. Henderson (1959) discussed the solubility of gypsum and anhydrite in saline solutions, proposing gypsum stability at maximum depths of 2000 feet (approximately 660 meters). The detection of anhydrite by XRD studies of sandstone samples (Díaz 2019) may indicate that at least part of the early eogenetic neoformed (i.e., precipitated) congruent gypsum could have dehydrated to form transformed anhydrite during late eogenesis to mesogenesis. Subsequently, anhydrite might have rehydrated and transformed into a second-generation gypsum cement with incongruent contacts during late mesogenesis to telogenesis.

Downloaded from http://pubs.geoscienceworld.org/sepm/jsedres/article-pdf/95/1/133/7113089/10.2110_jsr.2024.105.pdf
by Consejo Nacional de Investigaciones Cientificas y Tecnicas CONICET user

Kaolinite (Pore-Filling).—The most cited mechanism for kaolinite formation in the literature is the alteration of alkali feldspars, and it may occur at temperatures as low as 25 °C (Ehrenberg 1990; Walderhaug 1990) due to the percolation of meteoric waters in shallow-burial feldspathic sandstones. During this process, kaolinite precipitates directly on or surrounding clasts of alkali feldspar (Giles 1987; Stoessell and Pittman 1990; Lanson et al. 2002; Limarino et al. 2017a). A second type corresponds to kaolinite patches unrelated spatially to feldspar clasts. Milliken (2003) demonstrated that in some sandstone beds, the mass balance between alkali feldspars and authigenic kaolinite does not fit. Thus, the origin of Al^{3+} and silicic acid necessary for kaolinite formation must be assessed. Lanson et al. (2002) and Milliken (2003) indicate that aluminum ions would be provided by advection from the surrounding strata. Similarly, Limarino et al. (2017a) indicate that aluminum and silicic acid may come from transformation of volcanic glass inside the bed or from adjacent beds. This process occurs in tonstein levels, where kaolinite forms at the expense of volcanic glass (Lyons et al. 1992; Bohor and Triplehorn 1993). Although both processes operate during early diagenesis, the petrographic data presented here do not indicate that kaolinite is spatially restricted to alkali feldspars only. For that reason, we conclude that transformation of volcanic glass is the most probable process for kaolinite precipitation, providing the necessary Si, Al, and K ions.

Feldspar (Overgrowth on Feldspars Framework Seed Clasts).—The occurrence of albite overgrowth is volumetrically limited and restricted to alkali-feldspar clasts. Its origin may be related to feldspar albitization at temperatures as low as 60 °C and up to 100–130 °C (Worden and Morad 2000). Another albite source might include the heulandite–laumontite transformation, which occurs at temperatures ranging from 139 to 180 °C (Coombs 1954; Cho et al. 1987). Consequently, it is interpreted that this cement would have formed during late eogenesis or mesogenesis. The low albite content does not allow further interpretations regarding its time of precipitation.

The thermal history of Miocene–Pliocene basins above the Central Andean flat-slab subduction zone is still debatable. A Miocene geothermal gradient between 25 and 35 °C/km derived from thermochronometers proposed by Stevens Goddard and Carrapa (2018) contradicts the interpretations of Collo et al. (2011; 2017) that the base of the Vinchina depositional area could not have reached temperatures over 100 °C, suggesting a geothermal gradient between 12 and 18 °C/km. Stevens Goddard and Carrapa (2018) also quoted a personal communication to mention a modern geothermal gradient of ca. 24 $\pm$ 5 °C/km derived from a borehole (YPF.LR.G. es-1) near Guandacol town (La Rioja, Argentina; see Figure 1 for approximate borehole location) to support their findings. However, data provided to us by YPF for the above-mentioned borehole indicate a temperature of 165 °F (73.9 °C) recorded at a final 3700 m true vertical depth (TVD), which, after appropriate corrections (Deming and Chapman 1988) and considering a surface temperature between 10 and 20 °C, yield an approximate geothermal gradient between 14 and 17 °C/km. More recently, Wunderlin et al. (2021) presented apatite fission-track (AFT) and (U-Th)/He (AHe) data from two sections along the La Flecha–La Troya Sur creeks (La Troya depocenter, southwards of the studied Vinchina depocenter and near Guandacol), suggesting that the geothermal gradient varied from a maximum of $\sim$ 27 °C/km at about 15 Ma (age of lowermost VFm) to < 15 °C/km at 2 Ma (top of the overlying Toro Negro Formation). Later, Wunderlin et al. (2022) studied authigenic clay minerals from the same units deriving maximum temperatures between $\sim$ 60 and 80 °C for the lower to middle part of the VFm based on the presence of I/S R1 and the absence of I/S R3 phases in the middle part of VFm.

Papers published up to now intended to assess the geothermal gradient of the VFm and based their interpretations on cumulative present-day thicknesses without corrections for the compaction effect and consideration of any intervening period of uplift and erosion of part of the sedimentary pile. Although the cumulative thickness of the basin-fill units indicates that the base of the VFm may have been buried at 8 km, backstripping models suggest that by 5 Ma this surface may have reached a depth of 10 km (Stevens Goddard and Carrapa 2018). However, a recent study on the compactional fabrics of the VFm sandstones (Marenssi et al. 2023) has demonstrated that similar compactional characteristics are achieved at just 3.5 to 6 km of maximum burial depths in other basins, suggesting that repetitive episodes of deformation, uplift, and erosion (progressive unconformities) in the Vinchina Basin may have prevented the sedimentary pile from being deeply buried. In the studied samples, the laumontite–quartz pair in sandstones of the lower part of the VFm suggests that maximum temperatures may have reached a range between 139 and 180 °C (Coombs 1954; Cho et al. 1987). Additionally, mixed-layer I/S clays with R3 ordering type (Díaz 2019) indicate that burial temperatures reached 170–180 °C (Hoffman and Hower 1979). Considering a maximum burial depth of 10 km, the geothermal gradient may be somewhere between 13.9 and 18 °C/km (cf. Collo et al. 2017; Wunderlin et al. 2021, 2022), but considering just 6 km of burial, the geothermal gradient would range between 23 and 30 °C/km (cf. Stevens Goddard and Carrapa 2018). Note that both possibilities are in the range proposed by Wunderlin et al. (2021), who projected a progressive decrease in the geothermal gradient, which may have resulted from either the gradual horizontalization of the subducted plate from 15 Ma onwards or a delay in reaching new equilibrium conditions after the full plate horizontalization at that time. At this stage, our study suggests that an accurate maximum burial depth must be ascertained to calculate the Vinchina Basin's geothermal gradient.

CONCLUSIONS

The VFm sandstones exhibit a diverse array of twelve authigenic minerals, with zeolite, calcite, and gypsum being the most prevalent. Their distribution varies across the basin and in depth. Calcite dominates the northern section (Los Pozuelos), zeolite is more prominent in the central La Troya section, and gypsum is significant in the southern El Yeso section. These variations stem from a combination of environmental factors, framework clast compositions, and diagenetic processes.

The distribution of zeolite cement correlates with the quantity and nature of volcanic clasts. Analcime, abundant in the upper and lower sections, correlates with rhyolitic paleovolcanic clasts. Clinoptilolite–heulandite and laumontite, frequent in the central and northern areas, are linked to pulses of andesitic neovolcanic intercalations.

Carbonate cements dominate the coarser-grained (fluvial) facies in the northern region. In contrast, gypsum is more conspicuous in the finer-grained (lacustrine and playa-lake) facies in the basin's southern part. Accordingly, contents of clay-mineral rim cement increase from north to south as grain size decreases. The occurrence of smectite and I/S, the transformation of gypsum into anhydrite and clinoptilolite–heulandite to laumontite, the illitization of other clay minerals, the precipitation of different types of quartz cement, and the dissolution of clasts and previous cements are diagenetic processes related to sediment burial and the final rock uplift.

A diagenetic model is proposed to explain the various pathways observed from eogenesis to telogenesis, accounting for the compositional and textural characteristics of the sandstone cements in the VFm. Maximum temperatures may have been in the range of 139–162 °C during a relatively short residence time before uplift.

Several proposals have been made regarding the maximum temperatures reached during the Vinchina Formation's diagenesis. However, a robust depth–time model must still be established to determine the paleogeothermal

Downloaded from http://pubs.geoscienceworld.org/sepm/jsedres/article-pdf/95/1/133/7113089/10.2110_jsr.2024.105.pdf
by Consejo Nacional de Investigaciones Cientificas y Tecnicas CONICET user

gradient accurately. This model provides a more accurate understanding of the conditions influencing the formation of the authigenic minerals over time.

ACKNOWLEDGMENTS

This research was supported by ANPCyT PICT 1710/2018, PICT 03891/2020, and CONICET PIP 262/2015. We also recognize the support from Universidad de Buenos Aires and IGEBA (UBA-CONICET), Instituto y Museo de Ciencias Naturales (IMCN), and CIGEOBIO (UNSJ-CONICET). We thank Ricardo Calegari and Pablo Giampaoli (YPF S.A.) for providing information from the Guandacol borehole.

We would like to express our sincerest gratitude to the anonymous reviewers and JSR associate editor, Branimir Segvic, for their comprehensive review, constructive feedback, and valuable suggestions that have helped us to enhance the manuscript.

REFERENCES

Amidon, W.H., Ciccioli, P.L., Marenssi, S.A., Limarino, C.O., Fisher, G.B., Burbank, D. W., and Kylander-Clark, A., 2016, U-Pb ages of detrital and volcanic zircons of the Toro Negro Formation, northwestern Argentina: age, provenance and sedimentation rates: Journal of South American Earth Sciences, v. 70, p. 237–250.

Arigós, L., 1949, Descripción geológica de la Hoja 14c, Cerros de Cumichango (provincias de La Rioja y Catamarca): Instituto Nacional de Geología y Minería, Buenos Aires.

Barbera, G., Critelli, S., and Mazzoleni, P., 2011, Petrology and geochemistry of cretaceous sedimentary rocks of the Monte soro unit (Sicily, Italy): constraints on weathering, diagenesis and provenance: The Journal of Geology, v. 119, p. 51–68.

Beer, J.A., and Jordan, T.E., 1989, The effects of Neogene thrusting on deposition in the Bermejo Basin, Argentina: Journal of Sedimentary Petrology, v. 59, p. 330–345.

Bish, D.L., and Boak, J.M., 2001, Clinoptilolite–heulandite nomenclature: Reviews in Mineralogy and Geochemistry, v. 45, p. 207–216.

Blatt, H., 1979, Diagenetic processes in sandstones, *in* Scholle, P.A., and Schluger, P.R., eds., Aspects of Diagenesis: SEPM, Special Publication 26, p. 141–157.

Boggs, S., 2009, Petrology of Sedimentary Rocks: Cambridge University Press, 707 p.

Bohor, B.F., and Triplehorn, D.M., 1993, Tonsteins: altered volcanic-ash layers in coal bearing sequences: Geological Society of America, Special Paper 285, p. 1–44.

Boles, J.R., 1998, Carbonate cementation in Tertiary sandstones, San Joaquin basin, California, *in* Morad, S., ed., Carbonate Cementation in Sandstones: Distribution Patterns and Geochemical Evolution: International Association of Sedimentologists, p. 261–283.

Boles, J.R., and Coombs, D.S., 1975, Mineral reactions in zeolitic Triassic tuff, Hokonui Hills, New Zealand: Geological Society of America, Bulletin, v. 86, p. 163–173.

Boles, J.R., and Franks, S.G., 1979, Clay diagenesis in Wilcox sandstones of Southwest Texas: implications of smectite diagenesis on sandstone cementation: Journal of Sedimentary Petrology, v. 49, p. 55–70.

Burley, S.D., Mullis, J.T., and Matter, A., 1989, Timing diagenesis in the Tartan Reservoir (UK North Sea): constraints from combined cathodoluminescence microscopy and fluid inclusion studies: Marine and Petroleum Geology, v. 6, p. 98–120.

Carrigy, M.A., and Mellon, G.B., 1964, Authigenic clay mineral cements in Cretaceous and Tertiary sandstones of Alberta: Journal of Sedimentary Petrology, v. 34, p. 461–472.

Cerling, T.E., 1984, The stable isotopic composition of modern soil carbonate and its relationship to climate: Earth and Planetary Science Letters, v. 71, p. 229–240.

Chamley, H., 1989, Clay Sedimentology, Springer-Verlag, 623 p.

Chamley, H., 1994, Clay mineral diagenesis, *in* Parker, A., and Sellwood, B.W., eds., Quantitative Diagenesis: Recent Developments and Applications to Reservoir Geology: NATO, ASCI Science Series C, v. 453, p. 161–188.

Cho, M., Maruyama, S., and Liou, J.G., 1987, An experimental investigation of heulandite–laumontite equilibrium at 1000 to 2000 bar P fluid: Contributions to Mineralogy and Petrology, v. 97, p. 43–50.

Choquette, P.W., and Pray, L.C., 1970, Geologic nomenclature and classification of porosity in sedimentary carbonates: American Association of Petroleum Geologists, Bulletin, v. 54, p. 207–250.

Ciccioli, P.L., Limarino, C.O., Marenssi, S.A., Tedesco, A.M., and Tripaldi, A., 2011, Tectosedimentary evolution of the La Troya and Vinchina depocenters (northern Bermejo Basin, Tertiary), La Rioja, Argentina, *in* Salfity, J.A., and Marquillas, R.A., eds., Cenozoic Geology of the Central Andes of Argentina: Salta, SCS Publisher, p. 91–110.

Ciccioli, P.L., Limarino, C.O., Friedman, R., and Marenssi, S.A., 2014a, New high precision U-Pb ages for the Vinchina Formation: implications for the stratigraphy of the Bermejo Andean foreland basin (La Rioja province, western Argentina): Journal of South American Earth Sciences, v. 56, p. 200–213.

Ciccioli, P.L., Marenssi, S.A., and Limarino, C.O., 2014b, Petrology and provenance of the Toro Negro Formation (Neogene) of the Vinchina broken-foreland basin (Central Andes of Argentina): Journal of South American Earth Sciences, v. 49, p. 15–38.

Civitelli, M., Ravidà, D.C., Borrelli, M., Criniti, S., and Falsetta, E., 2023, Diagenesis and petrophysics of Miocene sandstones within southern Apennines foreland, Italy: Marine and Petroleum Geology, v. 155, 106411.

Collo, G., Dávila, F.M., Nobile, J., Astini, R.A., and Gehrels, G., 2011, Clay mineralogy and thermal history of the Neogene Vinchina Basin, central Andes of Argentina: analysis of factors controlling the heating conditions: Tectonics, v. 30, doi:10.1029/2010TC002841.

Collo, G., Dávila, F.M., Teixeira, W., Nóbile, J.C., Sant, L.G., and Carter, A., 2017, Isotopic and thermochronologic evidence of extremely cold lithosphere associated with a slab flattening in the Central Andes of Argentina: Basin Research, v. 29, p. 16–40.

Coombs, D.S., 1954, The nature and alteration of some Triassic sediments from Southland, New Zealand: Royal Society of New Zealand, Transactions, v. 82, p. 65–109.

Coombs, D.S., 1993, Dehydration veins in diagenetic and very-low-grade metamorphic rocks: features of the crustal seismogenic zone and their significance to mineral facies: Journal of Metamorphic Geology, v. 11, p. 389–399.

Coombs, D.S., Ellis, A.J., Fyfe, W.S., and Taylor, A.M., 1959, The zeolite facies, with comments on the interpretation of hydrothermal syntheses: Geochimica et Cosmochimica Acta, v. 17, p. 53–107.

Critelli, S., and Criniti, S., 2021, Sandstone petrology and provenance in fold–thrust belt and foreland basin system, *in* Al-Juboury, A.I., ed., Sedimentary Petrology: Implications in Petroleum Industry: Intech Open Access Publisher, Janeza Trdine, v. 9, p. 1–19, doi:10.5772/intechopen.96985.

Davies, D.K., and Ethridge, F.G., 1975, Sandstone composition and depositional environment: American Association of Petroleum Geologists, Bulletin, v. 59, p. 239–264.

Deconinck, J.F., and Chamley, H., 1995, Diversity of smectite origins in Late Cretaceous sediments: example of chalks from northern France: Clay minerals, v. 30, p. 365–379.

Deming, D., and Chapman, D.S., 1988, Heat flow in the Utah–Wyoming thrust belt from analysis of bottom-hole temperature data measured in oil and gas wells: Journal of Geophysical Research, Solid Earth, v. 93, p. 13,657–13,672.

Dickinson, W.R., 1970, Interpreting detrital modes of graywacke and arkose: Journal of Sedimentary Petrology, v. 40, p. 695–707.

Díaz, M., 2019, Modas detríticas, procedencia y diagénesis de la Formación Vinchina (Mioceno), Provincia de La Rioja, Argentina [Ph.D. Thesis]: Facultad de Ciencias Exactas y Naturales, Universidad de Buenos Aires, Ciudad Autónoma de Buenos Aires, 479 p.

Díaz, M., and Marenssi, S.A., 2020, Using sandstone and conglomerate petrofacies to unravel multiple provenance areas in broken-foreland basins: the Vinchina Formation (Miocene, NW Argentina) as a study case: Journal of South American Earth Sciences, v. 100, 102541.

Díaz, M., Marenssi, S.A., Limarino, C.O., and Schencman, L.J., 2019, Geoquímica de areniscas de la Formación Vinchina (Mioceno), La Rioja, Argentina: implicancias sobre procedencia, clima y marco tectónico: Revista de la Asociación Geológica Argentina, v. 76, p. 143–165.

Díaz, M., Marenssi, S.A., and Limarino, C.O., 2020, Non-parametric statistics as a tool for provenance analysis in gravel deposits: Vinchina Formation (Miocene, Argentine) as a study case: Latin American Journal of Sedimentology and Basin Analysis, v. 27, p. 163–183.

Dutta, P.K., and Suttner, L.J., 1986, Alluvial sandstone composition and paleoclimate; II, Authigenic mineralogy: Journal of Sedimentary Petrology, v. 56, p. 346–358.

Ehrenberg, S.N., 1990, Relationship between diagenesis and reservoir quality in sandstones of the Garn Formation, Haltenbanken, mid-Norwegian continental shelf: American Association of Petroleum Geologists, Bulletin, v. 74, p. 1538–1558.

Emmings, J.F., Dowey, P.J., Taylor, K.G., Davies, S.J., Vane, C.H., Moss-Hayes, V., and Rushton, J.C., 2020, Origin and implications of early diagenetic quartz in the Mississippian Bowland Shale Formation, Craven Basin, UK: Marine and Petroleum Geology, v. 120, 104567.

Folk, R.L., Andrews, P.B., and Lewis, D.W., 1970, Detrital sedimentary rock classification and nomenclature for use in New Zealand: New Zealand Journal of Geology and Geophysics, v. 13, p. 937–968.

Galloway, W.E., 1974, Deposition and diagenesis alteration of sandstone in northeast Pacific arc-related basins: implications for greywacke genesis: Geological Society of America, Bulletin, v. 85, p. 379–390.

Giles, M.R., 1987, Mass transfer and problems of secondary porosity creation in deeply buried hydrocarbon reservoirs: Marine and Petroleum Geology, v. 4, p. 188–204.

Haszeldine, R.S., Samson, I.M., and Cornford, C., 1984, Dating diagenesis in a petroleum basin, a new fluid inclusion method: Nature, v. 307, p. 354–357.

Henderson, G.G.L., 1959, Geology of the Stanford Range of the Rocky Mountains: British Columbia Department of Mines, Bulletin, 35, 93 p.

Hoffman, J., and Hower, J., 1979, Clay mineral assemblages as low grade metamorphic geothermometers: application to the thrust faulted disturbed belt of Montana, USA, *in* Scholle, P.A., and Schluger, P.R., eds., Aspects of Diagenesis: SEPM, Special Publication 26, p. 55–79.

Hower, J., Eslinger, E., Hower, M.E., and Perry, E.A., 1976, Mechanism of burial metamorphism of argillaceous sediment: 1. Mineralogical and chemical evidence: Geological Society of America, Bulletin, v. 87, p. 725–737.

Iijima, A., and Utada, M., 1966, Zeolites in sedimentary rocks, with reference to the depositional environments and zonal distribution: Sedimentology, v. 7, p. 327–357.

Downloaded from http://pubs.geoscienceworld.org/sepm/jsedres/article-pdf/95/1/133/7113089/10.2110_jsr.2024.105.pdf
by Consejo Nacional de Investigaciones Cientificas y Tecnicas CONICET user

Japas, M.S., Ré, G.H., Oriolo, S., and Vilas, J.F., 2015, Palaeomagnetic data from the Precordillera fold and thrust belt constraining Neogene foreland evolution of the Pampean flat-slab segment (Central Andes, Argentina), *in* Pueyo, E.L., Cifelli, F., Sussman, A.J., and Oliva-Urcia, B., eds., Palaeomagnetism in Fold and Thrust Belts: New Perspectives: Geological Society of London, Special Publication 425, p. 81–105.

Japas, M.S., Ré, G.H., Oriolo, S., and Vilas, J.F., 2016, Basement-involved deformation overprinting thin-skinned deformation in the Pampean flat-slab segment of the southern Central Andes, Argentina: Geological Magazine, v. 153, p. 1042–1065.

Jordan, T.E., Allmendinger, R.W., Damanti, J.F., and Drake, R.E., 1993, Chronology of motion in a complete thrust belt: the Precordillera, 30–31 S, Andes Mountains: The Journal of Geology, v. 101, p. 135–156.

Jordan, T.E., Schlunegger, F., and Cardozo, N., 2001, Unsteady and spatially variable evolution of the Neogene Andean Bermejo foreland basin, Argentina: Journal of South American Earth Sciences, v. 14, p. 775–798.

Kasprzyk, A., 1995, Gypsum-to-anhydrite transition in the Miocene of southern Poland: Journal of Sedimentary Research v. 65, p. 348–357.

Lanson, B., Beaufort, D., Berger, G., Bauer, A., Cassagnabere, A., and Meunier, A., 2002, Authigenic kaolin and illitic minerals during burial diagenesis of sandstones: a review: Clay minerals, v. 37, p. 1–22.

Limarino, C.O., Morelli, J.R., and Alonso, M.S., 1987, El color rojo de la sección superior del Grupo Paganzo (Pérmico): su origen y probable significado: Revista de la Asociación Argentina de Mineralogía, Petrología y Sedimentología, v. 18, p. 1–10.

Limarino, C., Tripaldi, A., Marenssi, S., Net, L., Ré, G., and Caselli, A., 2001, Tectonic control on the evolution of the fluvial systems of the Vinchina Formation (Miocene), northwestern Argentina: Journal of South American Earth Sciences, v. 14, p. 751–762.

Limarino, C.O., Ciccioli, P.L., and Marenssi, S.A., 2010, Análisis del contacto entre las formaciones Vinchina y Toro Negro (Sierra de los Colorados, provincia de La Rioja, Argentina), sus implicancias tectónicas: Latin American Journal of Sedimentology and Basin Analysis, v. 17, p. 113–132.

Limarino, C.O., Giordano, S.R., and Albertani, R.J.R., 2017a, Diagenetic model of the Bajo Barreal Formation (Cretaceous) in the southwestern flank of the Golfo de San Jorge Basin (Patagonia, Argentina): Marine and Petroleum Geology, v. 88, p. 907–931.

Limarino, C.O., Marenssi, S.A., Ciccioli, P.L., and Tedesco, A., 2017b, Estratigrafía Cenozoica de las cuencas de Antepaís de las Sierras Pampeanas noroccidentales y precordillera de La Rioja, *in* Muruaga, C., and Grosse, P., eds., Ciencias de la Tierra y Recursos Naturales: San Miguel de Tucumán, XX Congreso Geológico Argentino, p. 273–294.

Lyons, P.C., Outerbridge, W.F., Triplehorn, D.M., Evans, H.T., Congdon, R.D., Capiro, M., and Nash, W.P., 1992, An Appalachian isochron: a kaolinized Carboniferous air-fall volcanic-ash deposit (tonstein): Geological Society of America, Bulletin, v. 104, p. 1,515–1,527.

Marenssi, S.A., Net, L., Caselli, A., Tripaldi, A., and Limarino, C.O., 2000, Hallazgo de discordancias intraformacionales en la Formación Vinchina (Neógeno), quebrada de La Troya, La Rioja, Argentina: Revista de la Asociación Geológica Argentina v. 55, p. 414–418.

Marenssi, S.A., Ciccioli, P.L., Limarino, C.O., Schencman, L.J., and Diaz, M.Y., 2015, Using fluvial cyclicity to decipher the interaction of basement- and fold–thrust-belt tectonics in a broken foreland basin: Vinchina Formation (Miocene), northwestern Argentina: Journal of Sedimentary Research, v. 85, p. 361–380.

Marenssi, S.A., Limarino, C.O., Schencman, L.J., and Ciccioli, P.L., 2020, Tectonic and geomorphic controls on the lacustrine deposits of the Neogene Vinchina basin, northwestern Argentina: Journal of Sedimentary Research, v. 90, p. 250–267.

Marenssi, S.A., Díaz, M., and Limarino, C.O., 2023, Depositional and diagenetic controls on sandstone compactional fabrics in an Andean broken foreland basin, the Miocene Vinchina Formation, northwestern Argentina: Journal of South American Earth Sciences, v. 122, 104168.

McBride, E.F., 1989, Quartz cement in sandstones: a review: Earth-Science Reviews, v. 26, p. 69–112.

McKinley, J.M., Worden, R.H., and Ruffell, A.H., 1999, Smectite in sandstones: a review of the controls on occurrence and behaviour during diagenesis, *in* Worden, R.H., and Morad, S., eds., Clay Mineral Cements in Sandstones: The International Association of Sedimentologists, p. 109–128.

McLaughlin, O.M., Haszeldine, R.S., Fallick, A.E., and Rogers, G., 1994, The case of the missing clay, aluminium loss and secondary porosity, South Brae oilfield, North Sea: Clay Minerals, v. 29, p. 651–663.

Milana, J.P., Bercowski, F., and Jordan, T., 2003, Paleoambientes y magnetoestratigrafía del Neógeno de la Sierra de Mogna, y su relación con la Cuenca de Antepaís Andina: Revista de la Asociación Geológica Argentina v. 58, p. 447–473.

Milliken, K.L., 1998, Carbonate diagenesis in non-marine foreland sandstones at the western edge of the Alleghanian overthrust belt, Southern Appalachians, *in* Morad, S., ed., Carbonate Cementation in Sandstones: Distribution Patterns and Geochemical Evolution: The International Association of Sedimentologists, p. 87–105.

Milliken, K.L., 2003, Late diagenesis and mass transfer in sandstone shale sequences, *in* Holland, H.D., and Turekian, K.K., eds., Treatise on Geochemistry: Pergamon, p. 159–190, doi:10.1016/B0-08-043751-6/07091-2.

Moore, D.M., and Reynolds, R.C., Jr., 1997, X-Ray Diffraction and the Identification and Analysis of Clay Minerals, 2nd Edition: Oxford, Oxford University Press, 378 p.

Morad, S., 1998, Carbonate cementation in sandstones: distribution patterns and geochemical evolution, *in* Morad, S., ed., Carbonate Cementation in Sandstones: Distribution Patterns and Geochemical Evolution: The International Association of Sedimentologists, v. 26, p. 1–26, doi:10.1002/9781444304893.ch1.

Morad, S., Ketzer, J.M., and De Ros, L.F., 2000, Spatial and temporal distribution of diagenetic alterations in siliciclastic rocks: implications for mass transfer in sedimentary basins: Sedimentology, v. 47, p. 95–120.

Morad, S., Al-Ramadan, K., Ketzer, J.M., and De Ros, L.F., 2010, The impact of diagenesis on the heterogeneity of sandstone reservoirs: a review of the role of depositional facies and sequence stratigraphy: American Association of Petroleum Geologists, Bulletin, v. 94, p. 1267–1309.

Murray, R.C., 1964, Origin and diagenesis of gypsum and anhydrite: Journal of Sedimentary Petrology, v. 34, p. 512–523.

Pagel, M., 1975, Détermenation de conditions physicochimiques de la silicification diagénetique des grés Athabasca (Canada) au moyen de inclusions fluides: Academie de Sciences, Comptes Rendus, Serie II, v. 280, p. 2301–2304.

Pettijohn, F.J., Potter, P.E., and Siever, R., 1972, Sand and Sandstone, Petrographic Classification and Glossary: Springer, p. 149–174.

Pollastro, R.M., 1993, Considerations and applications of the illite/smectite geothermometer in hydrocarbon-bearing rocks of Miocene to Mississippian age: Clays and Clay minerals, v. 41, p. 119–133.

Posnjak, E., 1938, The system $CaSO_4$–H_20: American Journal of Science v. 235, p. 247–272.

Prajapati, N., Abad Gonzalez, A., Selzer, M., Nestler, B., Busch, B., and Hilgers, C., 2020, Quartz cementation in polycrystalline sandstone: Insights from phase-field simulations: Journal of Geophysical Research, Solid Earth, v. 125, e2019JB019137.

Ramos, V.A., 1970, Estratigrafía y estructura del Terciario en la sierra de los Colorados (Provincia de La Rioja), República Argentina: Revista de la Asociación Geológica Argentina, v. 25, p. 359–382.

Reynolds, R.C., 1980, Interstratified clay minerals, *in* Brindley, G.W., and Brown, G., eds., Crystal Structures of Clay Minerals and Their X-Ray Identification: Mineralogical Society of London, p. 249–303.

Saigal, G.C., and Bjørlykke, K., 1987, Carbonate cements in clastic reservoir rocks from offshore Norway: relationships between isotopic composition, textural development and burial depth, *in* Marshal, J.D., ed., Diagenesis of Sedimentary Sequences: Geological Society of London, Special Publication, v. 36, p. 313–324, doi:10.1144/GSL.SP.1987.036.01.22.

Schencman, L.J., 2016, Arquitectura de sistemas fluviales, modelos depositacionales y estratigrafía secuencial en cuencas de antepaís: la Formación Vinchina, un caso de estudio, [Ph.D. Thesis]: Universidad de Buenos Aires, 272 p.

Schencman, L.J., Marenssi, S.A., and Díaz, M., 2018, Evolución paleoambiental de la Formación Vinchina (Mioceno) en la sierra de Los Colorados, La Rioja, Argentina: Revista de la Asociación Geológica Argentina, v. 75, p. 17–38.

Stevens Goddard, A.L., and Carrapa, B., 2018, Using basin thermal history to evaluate the role of Miocene–Pliocene flat-slab subduction in the southern Central Andes (27 ° S–30 ° S): Basin Research, v. 30, p. 564–585.

Stoessell, R.K., and Pittman, E.D., 1990, Secondary porosity revisited: the chemistry of feldspar dissolution by carboxylic acids and anions: American Association of Petroleum Geologists, Bulletin v. 74, p. 1795–1805.

Suttner, L.J., and Dutta, P.K., 1986, Alluvial sandstone composition and paleoclimate; I, framework mineralogy: Journal of Sedimentary Petrology, v. 56, p. 329–345.

Tripaldi, A., Net, L., Limarino, C., Marenssi, S., Ré, G., and Caselli, A., 2001, Paleoambientes sedimentarios y procedencia de la Formación Vinchina, Mioceno, noroeste de la provincia de La Rioja: Revista de la Asociación Geológica Argentina, v. 56, p. 443–465.

Turner, J.C.M., 1964, Descripción geológica de la Hoja 15c, Vinchina, provincia de La Rioja: Buenos Aires, Dirección Nacional de Geología y Minería, Boletín 100.

Tyrell, G.W., and Peacock, M.A., 1926, The petrography of Iceland: Royal Society of Edinburgh, Transactions, v. 55, p. 62–63.

Utada, M., 1965, Zonal distribution of authigenic zeolites in the Tertiary pyroclastic rocks in Mogami district, Yamagata Prefecture: University of Tokyo, Scientific Papers of the College of General Education, v. 15, p. 173–216.

Valdes, P.J., Scotese, C.R., and Lunt, D.J., 2021, Deep ocean temperatures through time: Climate of the Past, v. 17, p. 1483–1506, doi:10.5194/cp-17-1483-2021.

Walderhaug, O., 1990, A fluid inclusion study of quartz-cemented sandstones from offshore mid-Norway: possible evidence for continued quartz cementation during oil emplacement: Journal of Sedimentary Petrology, v. 60, p. 203–210.

Walker, T.R., 1967, Formation of red beds in modern and ancient deserts: Geological Society of America, Bulletin, v. 78, p. 353–368.

Welton, J.E., 2003, SEM petrology atlas: American Association of Petroleum Geologists, Methods in Exploration Series, v. 8, p. 68–84.

Westcot, D.W., and Wierenga, P.J., 1974, Transfer of heat by conduction and vapor movement in a closed soil system: Soil Science Society of America, Journal, v. 38, p. 9–14.

Wilson, M.D., and Stanton, P.T., 1994, Diagenetic mechanisms of porosity and permeability reduction and enhancement, *in* Wilson, M.D., ed., Reservoir Quality Assessment and Prediction in Clastic Rocks; SEPM, Short Course Notes, v. 30.

Worden, R.H., and Burley, S.D., 2003, Sandstone diagenesis: the evolution of sand to stone, *in* Burley, S.D., and Worden, R.H., eds., Sandstone Diagenesis: Recent and Ancient: International Association of Sedimentologists, p. 1–44.

Downloaded from http://pubs.geoscienceworld.org/sepm/jsedres/article-pdf/95/1/133/7113089/10.2110_jsr.2024.105.pdf
by Consejo Nacional de Investigaciones Cientificas y Tecnicas CONICET user

Worden, R.H., and Morad, S., 2000, Quartz cementation in oil field sandstones: a review of the key controversies, *in* Worden, R.H., and Morad, S., eds., Quartz Cementation in Sandstones: International Association of Sedimentologists, p. 1–20.

Wunderlin, C., Collo, G., Parra, M., Ezpeleta, M., Nassif, F.S., Flores, M., Sobel, E.R., and Glodny, J., 2021, New thermocronological data of the Cretaceous–Cenozoic clastic sequences from the Vinchina basin: linkage between burial, exhumation and thermal flow variations: Journal of South American Earth Sciences, v. 105, 102964.

Wunderlin, C.A., Collo, G., Ezpeleta, M., Carbonell, V.V.R., Nóbile, J.C., Ciccioli, P.L., and Faudone, S., 2022, Authigenic and detrital clay minerals as indicators of paleoenvironmental and postdepositional evolution in a Cretaceous–Cenozoic succession from Argentine Central Andes: Sedimentary Geology, v. 437, 106179.

Received 9 August 2024; accepted 15 November 2024.

Downloaded from http://pubs.geoscienceworld.org/sepm/jsedres/article-pdf/95/1/133/7113089/10.2110_jsr.2024.105.pdf
by Consejo Nacional de Investigaciones Cientificas y Tecnicas CONICET user